Astronomy & Astrophysics manuscript no. main ©ESO 2020
April 15, 2020

Precise mass and radius of a transiting super-Earth planet orbiting the M dwarf TOI-1235: a planet in the radius gap?

P. Bluhm[1], R. Luque[2,3], N. Espinoza[4], E. Pallé[2,3], J. A. Caballero[5], S. Dreizler[7], J. H. Livingston[8], S. Mathur[2,3], A. Quirrenbach[1], S. Stock[1], V. Van Eylen[9], G. Nowak[2,3], E. D. López[10,11], Sz. Csizmadia[12], M. R. Zapatero Osorio[13], P. Schöfer[7], J. Lillo-Box[5], M. Oshagh[2,3], P. J. Amado[6], D. Barrado[5], V. J. S. Béjar[2,3], B. Cale[14], P. Chaturvedi[15], C. Cifuentes[5], W. D. Cochran[16], K. A. Collins[17], K. I. Collins[14], M. Cortés-Contreras[5], E. Díez Alonso[18,19], M. El Mufti[14], A. Ercolino[20], M. Fridlund[21,22], E. Gaidos[23], R. A. García[24,25], E. González-Álvarez[13], L. González-Cuesta[2,3], P. Guerra[26], A. P. Hatzes[15], T. Henning[27], E. Herrero[28,29], D. Hidalgo[2,3], G. Isopi[20], S. V. Jeffers[7], J. M. Jenkins[30], E. L. N. Jensen[31], P. Kábath[32], J. Kemmer[1], J. Korth[33], D. Kossakowski[27], M. Kürster[27], M. Lafarga[28,29], F. Mallia[20], D. Montes[34], J. C. Morales[28,29], M. Morales-Calderón[5], F. Murgas[2,3], N. Narita[2,35,36,37], P. Plavchan[14], V. M. Passegger[38,39], S. Pedraz[40], H. Rauer[12,41,42], S. Redfield[43], S. Reffert[1], A. Reiners[7], I. Ribas[28,29], G. R. Ricker[44], C. Rodríguez-López[6], A. R. G. Santos[45], S. Seager[44,46,47], Y. Shan[7], M. Schlecker[27], A. Schweitzer[38], M. G. Soto[48], J. Subjak[32], L. Tal-Or[49,7], T. Trifonov[27], S. Vanaverbeke[50,51], R. Vanderspek[44], J. Wittrock[14], M. Zechmeister[7], and F. Zohrabi[52]

(Affiliations after the references)

Received dd April 2020 / Accepted dd Month 2020

ABSTRACT

We report the confirmation of a transiting planet around the bright, inactive M0.5 V star TOI-1235 (TYC 4384–1735–1, $V = 11.5$ mag), whose transit signal was detected in the photometric time series of Sectors 14, 20, and 21 of the *TESS* space mission. We confirm the planetary nature of the transit signal, which has a period of 3.44 d, by using precise radial velocity measurements with CARMENES and HARPS-N spectrographs. A comparison of the properties derived for TOI-1235 b's with theoretical models reveals that the planet has a rocky composition, with a bulk density slightly higher than Earth's. In particular, we measure a mass of $M_p = 5.9 \pm 0.6\,M_\oplus$ and a radius of $R_p = 1.69 \pm 0.08\,R_\oplus$, which together result in a density of $\rho_\mathrm{p} = 6.7^{+1.3}_{-1.1}$ g cm^{-3}. When compared with other well-characterized exoplanetary systems, the particular combination of planetary radius and mass puts our discovery in the radius gap, a transition region between rocky planets and planets with significant atmospheric envelopes, with few known members. While the exact location of the radius gap for M dwarfs is still a matter of debate, our results constrain it to be located at around 1.7 $R_\oplus$ or larger at the insolation levels received by TOI-1235 b ($\sim$60 $S_\oplus$), which makes it an extremely interesting object for further studies of planet formation and atmospheric evolution.

Key words. planetary systems – techniques: photometric – techniques: radial velocities – stars: individual: TOI-1235 – stars: late-type

1. Introduction

Currently, over 4000 exoplanetary systems have been discovered orbiting stars other than the Sun[1], with the majority of the planets having sizes between that of the Earth and Neptune (Batalha et al. 2013). Most of these systems were discovered by the *Kepler* mission (Borucki et al. 2010; Borucki 2016), which by design focused its transit survey on stars of spectral types F, G, and K. In order to understand the processes involved in how planets form and evolve, it is useful to compare how the outcomes vary across different environments, e.g., consider planetary demographics across a range of host star contexts. No picture of exoplanet populations can be complete without a sizable and representative sample of planetary systems around M dwarfs – the most common type of stars in our Galaxy (Chabrier 2003; Henry et al. 2006). Indeed, the occurrence rate of small planets orbiting M dwarfs appears to increase toward late spectral subtypes at all orbital periods (Bonfils et al. 2013; Dressing & Charbonneau 2015; Mulders et al. 2015; Gaidos et al. 2016). In spite of this abundance, the number of exoplanets with M star hosts having precisely known radii and masses is still small, as these stars are intrinsically faint, and only the closest ones are well-suited for detailed follow-up and characterization.

One of the most interesting features observed in the distribution of sizes of small ($R < 4\,R_\oplus$) exoplanets has been its bimodal nature, and is commonly referred as the "radius gap". It separates the planets with radii slightly smaller than Neptune (2–4 $R_\oplus$) from those with radii slightly larger than Earth (1–2 $R_\oplus$). While the former are believed to bear a significant contribution of water (Morbidelli 2018), the latter are thought to be predominantly rocky. Although it was theoretically predicted (e.g., Owen & Wu 2013; Jin et al. 2014; López & Fortney 2014; Chen & Rogers 2016), the radius gap was observationally characterized only relatively recently (e.g., Fulton et al. 2017; Zeng et al. 2017; Van Eylen et al. 2018; Berger et al. 2018; Fulton & Petigura 2018), owing to an improvement in the planetary radius determination through more accurate models and stellar radii thanks to new high-resolution stellar spectroscopy (Schweitzer et al. 2019), asteroseismology (García & Ballot 2019), and pre-

---

[1] `https://exoplanetarchive.ipac.caltech.edu/`, `http://exoplanet.eu/`

Table 1. *TESS* observations of TOI-1235.

Sector	Camera	CCD	Start date	End date
14	4	3	18 July 2019	15 August 2019
20	2	1	24 December 2019	21 January 2020
21	2	2	21 January 2020	18 February 2020

cise parallactic distances from the *Gaia* mission (Gaia Collaboration et al. 2018).

Presently, there are two classes of models to explain this radius gap: photo-evaporation models, which posit that planets that end up below the radius gap lost their atmospheres due to X-ray and ultraviolet radiation from the star (XUV; e.g., Owen & Wu 2013; López & Fortney 2013; Jin et al. 2014; Chen & Rogers 2016; Owen & Wu 2017), and core-powered mass loss models, which also propose that close-in planets below the radius gap have lost their atmospheres, but conjecture that mass-loss is actually powered by heat from the planetary core (Ginzburg et al. 2016, 2018; Gupta & Schlichting 2019). These two mechanisms have different dependencies on the stellar type of the host stars and the total irradiation that the planets receive (Wu 2019; Gupta & Schlichting 2020), which means that the actual location of the radius gap can indeed change with those parameters. Since most of the existing studies are based on *Kepler* samples or sub-samples – i.e., samples heavily focused on F, G and K-type stars – transiting exoplanetary systems around M-type stars have a huge potential to help constrain the most important mechanism(s) producing this bimodal distribution (see, e.g., Hirano et al. 2018). Measuring the planetary mass, in turn, allows us to have a peek at the bulk composition of the exoplanets, which delivers a clearer picture of the underlying nature of the radius gap.

The *Transiting Exoplanet Survey Satellite* (*TESS*; Ricker et al. 2015) has proven to be a prime instrument to detect and characterize small planets orbiting bright stellar hosts. Having completed its first year of monitoring, it has contributed to the detection and confirmation of more than 40 new transiting exoplanetary systems (see, e.g., Huang et al. 2018; Gandolfi et al. 2018; Luque et al. 2019; Esposito et al. 2019; Wang et al. 2019; Crossfield et al. 2019; Günther et al. 2019; Gilbert et al. 2020; Espinoza et al. 2020; Silverstein et al. 2020; Nowak et al. 2020), many of which are small planets orbiting low-mass M stars. Here we report on a very interesting addition to this growing sample of *TESS* transiting exoplanet discoveries around M dwarfs: a transiting super-Earth that appears to be right in the radius gap for low-mass stars orbiting the early M dwarf TOI-1235.

The paper is organized as follows. Section 2 presents the *TESS* photometry used in this work, along with ground-based observations of the star, including high-resolution spectroscopy, lucky and speckle imaging, and photometric variability monitoring. Section 3 presents the stellar properties of the host star, newly derived and collected from the literature. In Section 4 we present our analysis of the available data to constrain the planetary properties of the system. In Section 5 we discuss our results, with an emphasis on the location of the planet in the mass-radius diagram and its composition, and, finally, Section 6 shows our conclusions.

2. Data

2.1. TESS photometry

TOI-1235 (TIC 103633434) was observed by *TESS* in 2 min short-cadence integrations in Sectors 14, 20, and 21 during the *TESS* primary mission (see Table 1), and was announced on September 13, 2019 as a *TESS* object of interest (TOI) via the dedicated MIT *TESS* data alerts public website[2]. We downloaded the corresponding light curve produced by the Science Processing Operations Center (SPOC; Jenkins et al. 2016) at NASA Ames Research Center from the Mikulski Archive for Space Telescopes[3]. SPOC provides simple aperture photometry (SAP) and photometry corrected for systematics (PDC, Smith et al. 2012; Stumpe et al. 2012, 2014), which is optimized for *TESS* transit searches. Figure 1 shows the PDC data for the three *TESS* sectors with the best-fit model (for details see Sect. 4.4). The transit signal has a period of 3.4431±0.0008 d, and a depth of 0.91±0.08 mmag, corresponding to a planet radius of about 2 $R_\oplus$.

2.2. High-resolution spectroscopy

2.2.1. CARMENES

CARMENES[4] (Quirrenbach et al. 2014, 2018) is a high-resolution spectrograph mounted on the 3.5 m telescope at the Observatorio de Calar Alto in Almería, Spain. It splits the incoming light into two channels, one that operates in the optical (VIS: 0.52–0.96 µm, $\mathcal{R}$ = 94 600) and the other in the near infrared (NIR: 0.96–1.71 µm, $\mathcal{R}$ = 80 400). TOI-1235 was observed 40 times with CARMENES between 09 November 2019 and 18 February 2020, overlapping with the *TESS* Sector 20 and 21 observations. We used an exposure time of 1800 s and followed the standard data flow of the CARMENES guaranteed time observations. In particular, we reduced the VIS spectra with `CARACAL` (Zechmeister et al. 2014) and determined the corresponding radial velocities and spectral activity indices (see Sect. 4.3) with `SERVAL` (Zechmeister et al. 2018). We corrected the radial velocities for barycentric motion, instrumental drift, secular acceleration and nightly zero-points (see Trifonov et al. 2018, Kaminski et al. 2018, and Tal-Or et al. 2019 for details). The CARMENES radial velocities and their uncertainties are listed in Table A.2.

2.2.2. HARPS-N

HARPS-N (Cosentino et al. 2012) is a high-resolution spectrograph mounted on the Italian 3.58 m Telescopio Nazionale Galileo at the Observatorio del Roque de los Muchachos, La Palma, Spain. HARPS-N covers the optical wavelength regime between 0.38 μm and 0.69 μm with a spectral resolution of $\mathcal{R}$ = 115 000. The precision and stability of HARPS-N is comparable to its sister instrument HARPS on the ESO 3.6 m telescope and, therefore, to CARMENES (Trifonov et al. 2018; Perger et al. 2019). TOI-1235 was observed 21 times between 14 January 2020 and 26 February 2020 with HARPS-N[5], also overlapping with *TESS* Sector 20 and 21. Just as with the CARMENES data,

---

[2] `https://tess.mit.edu/alerts/`

[3] `https://mast.stsci.edu`

[4] Calar Alto high-Resolution search for M dwarfs with Exoearths with Near-infrared and optical Echelle Spectrographs: `http://carmenes.caha.es`

[5] HARPS-N data: 15 RVs were obtained from the Spanish CAT19A-162 program (PI: Nowak) and 6 RVs from ITP 19-1 program (PI: Pallé).

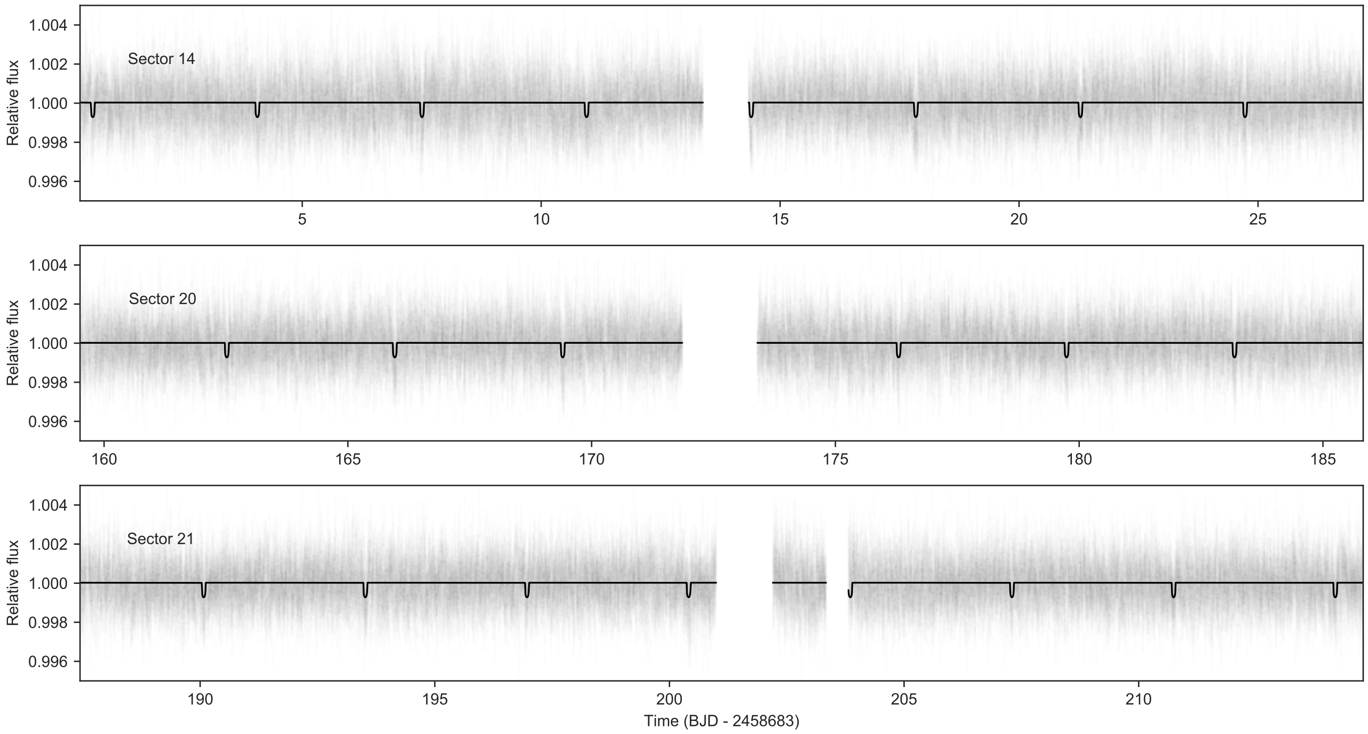

Fig. 1. *TESS* transit photometry for the three sectors (grey points) with the best-fit `juliet` model (black line; see Sect. 4.4 for details on the modelling).

we determined the radial velocities and Hα spectral activity index with `SERVAL`, which are listed in Table A.2.

2.3. High-resolution imaging

2.3.1. AstraLux

We observed TOI-1235 with the high spatial resolution camera and lucky imager AstraLux (Hormuth et al. 2008) on the 2.2 m telescope at the Observatorio de Calar Alto in Almería, Spain. The observations were carried out in the z' band on 30 October 2019 under good weather conditions with a mean seeing of 1.0 arcsec. We obtained 96 000 frames of 10 ms in a $6.0 \times 6.0\,\mathrm{arcsec}^2$ window. With the observatory pipeline, we selected the 5 % frames with the highest Strehl ratio (Strehl 1902), aligned them, and stacked them for a final high-spatial resolution image.

2.3.2. NESSI

On 14 October of 2019 we observed TOI-1235 with the NASA Exoplanet Star and Speckle Imager (NESSI; Scott et al. 2018; Scott & Howell 2018) on the 3.5 m WIYN telescope at the Kitt Peak National Observatory in Arizona, USA. We observed nearby point-source calibrator stars and reduced the data following Howell et al. (2011). The high-speed electron-multiplying CCDs of NESSI capture images at 25 Hz simultaneously in two bands centered at 562 nm and 832 nm. Finally, we obtained two $4.6 \times 4.6\,\mathrm{arcsec}^2$ reconstructed images, one for each passband.

2.4. Ground-based photometry

Additional photometric data for TOI-1235 were taken on 31 December 2019 with one of the 1 m telescopes of the Las Cumbres Observatory Global Telescope (LCOGT; Brown et al. 2013) Network at the McDonald Observatory in Texas, USA. We used the `TESS Transit Finder`, which is a customized version of the `Tapir` software package (Jensen 2013), to schedule a full transit observation. We used the zs (short z') band and an aperture radius of 7.0 arcsec for the photometry extraction. A total of 358 photometric measurements were obtained with a cadence of 56 s and a median precision of 1100 ppm per point. The images were calibrated using the standard LCOGT `Banzai` pipeline (McCully et al. 2018), and the photometric data were extracted using the `AstroImageJ` software package (Collins et al. 2017).

We also observed a TOI-1235 transit on 29 March 2020 with the 0.8 m Telescopi Joan Oró (TJO) at the Observatori Astronòmic del Montsec in Lleida, Spain. We obtained a total of 221 images with the Johnson R filter using the LAIA imager, a $4\mathrm{k} \times 4\mathrm{k}$ CCD with a field of view of 30 arcmin and a scale of $0.4\,\mathrm{arcsec\,pixel}^{-1}$. The observations were affected by poor weather conditions, and the photometry was extracted and analyzed with `AstroImageJ`. Although we did not use this photometry in the joint modelling due to the poor photometric precision, it was anyways useful as an independent confirmation that the transit event indeed ocurred on the target star, as the TJO photometry for all *Gaia* DR2 sources within 2.5 arcmin of the target ruled out the possibility that the *TESS* transit signal was produced by any of these stars being short-period eclipsing binary contaminants.

Finally, we searched for public time series data of wide-area photometric surveys and databases as in Díez Alonso et al. (2019). In particular, we retrieved light curves from the All-Sky

Table 2. Descriptions of data from public ground-based surveys used in this work[a].

Survey	Band	Start date	End date	N	Δt (d)	$\overline{m}$ (mag)	σ_m (mag)	$\overline{\delta m}$ (mag)
ASAS-SN	g'	29 October 2017	24 March 2020	603[b]	877	12.255	0.026	0.010
	V	28 January 2012	26 November 2018	713[b]	2494	11.572	0.018	0.009
NSVS	Clear	04 June 2018	20 May 2019	111	359	11.027	0.024	0.011
Catalina[c]	Clear	02 February 2006	18 April 2013	43	2632	10.761	0.089	0.050

Notes. (a) Number of collected data points. (b) After discarding 20 g' and 10 V dubious data points (with poor quality flags). (c) Data set eventually not used.

Automated Survey for SuperNovae (ASAS-SN; Shappee et al. 2014; Kochanek et al. 2017) in the g' and V bands, and the Northern Sky Variability Survey (NSVS; Woźniak et al. 2004), and the Catalina Sky Survey (Drake et al. 2009) in white light. Table 2 summarizes the three public data sets. The Catalina data set is much noisier, sparser, and shorter than the others, so we did not use it in our analysis. In addition, we did not find data on TOI-1235 in other photometric surveys, such as MEarth (Irwin et al. 2011), SuperWASP (Pollacco et al. 2006, including unpublished data), ASAS (Pojmański 1997), and HATNet (Bakos et al. 2004). At last, TOI-1235 was not labeled as a variable star in the ATLAS survey (Heinze et al. 2018).

Table 3. Stellar parameters of TOI-1235.

Parameter	Value	Reference
	Name and identifiers	
Name	TYC 4384–1735–1	Høg00
Karmn	J10088+692	AF15
TOI	1235	ExoFOP-TESS
TIC	103633434	Sta18
	Coordinates and spectral type	
α (J2000)	10:08:51.81	*Gaia* DR2
δ (J2000)	+69:16:35.6	*Gaia* DR2
Sp. type	M0.5 V	Lep13
G [mag]	10.8492 ± 0.0005	*Gaia* DR2
J [mag]	8.711 ± 0.020	Skr06
	Parallax and kinematics	
ϖ [mas]	25.202 ± 0.030	*Gaia* DR2
d [pc]	39.680 ± 0.048	*Gaia* DR2
$\mu_\alpha \cos\delta$ [mas a^{-1}]	$+196.631 \pm 0.040$	*Gaia* DR2
μ_δ [mas a^{-1}]	$+17.364 \pm 0.047$	*Gaia* DR2
γ [km s^{-1}]	-27.512 ± 0.018	This work
U [km s^{-1}]	$+45.98 \pm 0.04$	This work
V [km s^{-1}]	-4.29 ± 0.01	This work
W [km s^{-1}]	$+1.73 \pm 0.03$	This work
Gal. population	Thin disk	This work
	Photospheric parameters	
$T_{\rm eff}$ [K]	3997 ± 51	This work
$\log g$	4.64 ± 0.04	This work
[Fe/H]	$+0.33 \pm 0.16$	This work
$v \sin i_\star$ [km s^{-1}]	< 2.0	This work
	Physical parameters	
$L_\star$ [$10^{-4} L_\odot$]	883 ± 3	This work
$M_\star$ [$M_\odot$]	0.630 ± 0.024	This work
$R_\star$ [$R_\odot$]	0.619 ± 0.019	This work
	Activity and age	
pEW(Hα) [Å]	$+0.97 \pm 0.06$	This work
$\log R'_{\rm HK}$	-4.728 ± 0.015	This work
$S_{\rm MWO}$	1.005 ± 0.029	This work
Age (Ga)	0.6–10	This work

References. AF15: Alonso-Floriano et al. (2015); *Gaia* DR2: Gaia Collaboration et al. (2018); Høg00: Høg et al. (2000); Lep13: Lépine et al. (2013); Skr06: Skrutskie et al. (2006); Sta18: Stassun et al. (2018). Schf19: Schöfer et al. (2019)

3. Stellar properties

The star TOI-1235 (TYC 4384–1735–1) has been included in only a few proper-motion surveys (Høg et al. 2000; Lépine & Shara 2005; Kirkpatrick et al. 2016) and catalogs of nearby M dwarfs that could host exoplanets (Lépine & Gaidos 2011; Frith et al. 2013; Gaidos et al. 2014). As indicated by its Tycho-2 identifier, TOI-1235 is a relatively nearby ($d \approx 39.6$ pc), bright ($V \approx 11.5$ mag) star. Lépine et al. (2013) and Gaidos et al. (2014) reported spectral types M0.5 V and M1.0 V and effective temperatures $T_{\rm eff}$ of 3660 K and 4060 K, respectively. Gaidos et al. (2014) also derived stellar radius $R_\star$ and bolometric luminosity $L_\star$, which are consistent with the determinations by Gaia Collaboration et al. (2018), mass $M_\star$, and pseudo-equivalent width of the Hα line, pEW(Hα).

We re-determined all stellar parameters for this early M dwarf. In particular, we measured $T_{\rm eff}$, surface gravity $\log g$, and iron abundance [Fe/H] from the stacked CARMENES VIS spectra by fitting them with a grid of PHOENIX-SESAM models (Husser et al. 2013) as in Passegger et al. (2018), the rotational velocity $v \sin i$ with the cross-correlation method as in Reiners et al. (2018), and the stellar luminosity $L_\star$ by integrating the spectral energy distribution as in Cifuentes et al. (2020). For that, we used photometric data in 17 passbands from the optical blue Tycho-2 B_T (Høg et al. 2000) to the mid-infrared AllWISE $W4$ (Cutri & et al. 2014), the Virtual Observatory Spectral energy distribution Analyzer (VOSA; Bayo et al. 2008), and the BT-Settl CIFIST theoretical models, which were used to extrapolate the spectral energy distribution at ranges bluer than B_T and redder than $W4$. The photospheric contributions to the total stellar flux of an M0.5 V star in those ranges are <0.5 % and < 0.004 %, respectively, so the $L_\star$ determination was model-independent at the >99.5 % level. Next, we determined $R_\star$ via the Stefan–Boltzmann law, $L_\star = 4\pi {R_\star}^2 \sigma T_{\rm eff}^4$, and $M_\star$ with the mass-radius relation derived from main-sequence eclipsing binaries by Schweitzer et al. (2019). All re-determined parameters ($T_{\rm eff}$, $L_\star$, $R_\star$, $M_\star$) match within 1σ the values published by Gaidos et al. (2014) and Gaia Collaboration et al. (2018). Furthermore, we used the precise astrometric data of *Gaia* DR2, the absolute radial velocity measured on the stacked CARMENES spectra as in Lafarga et al. (2020), and the prescription of Johnson & Soderblom (1987) for measuring the Galactocentric space velocities UVW. Using this kinematic information with the BANYAN Σ tool (Gagné et al. 2018), we classified TOI-1235 as a field star

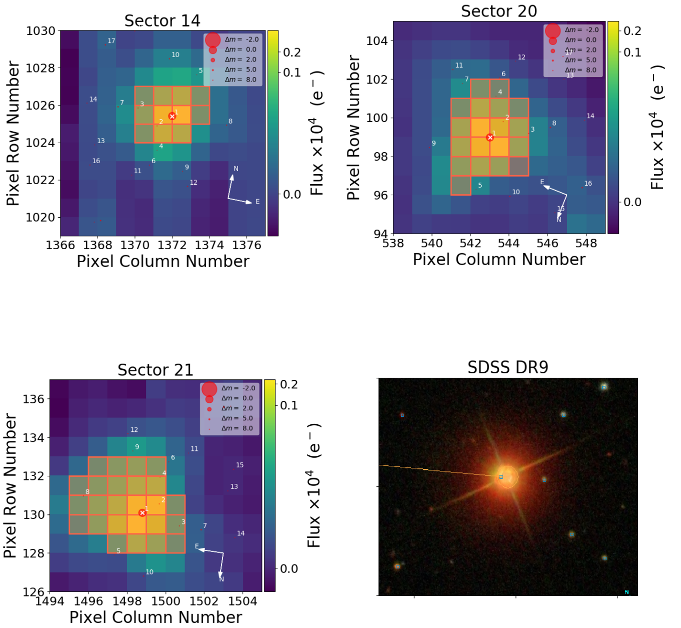

Fig. 2. Target pixel files (TPF) of TOI-1235 in *TESS* Sectors 14, 20, and 21. The electron counts are color-coded. The red bordered pixels are used in the simple aperture photometry (SAP). The size of the red circles indicates the *TESS* magnitudes of all nearby stars and TOI-1235 (circle #1 marked with «×»). *Bottom right*: false-color, 2 × 2 arcmin^2 Sloan Digital Sky Survey DR9 image centered on TOI-1235 (north is up, east is left).

in the Galactic thin disk not associated with any young stellar kinematic group.

Finally, we determined key indicators of stellar activity. First, we measured the Mount Wilson S index, $S_{\rm MWO}$, with the `Yabi` data environment on the HARPS-N spectra, from which we derived $\log R'_{\rm HK}$ using the formulae of Astudillo-Defru et al. (2017) and $V - K_s = 3.602\pm0.0.059$ mag. Next, we measured pEW(Hα) on the CARMENES stacked spectrum following Schöfer et al. (2019), which was identical within 2σ to the pEW(Hα) = +0.74±0.11 Å measured by Gaidos et al. (2014) in April 2009. These three indicators make TOI-1235 one of the least active stars for its spectral type (Wright et al. 2004; Astudillo-Defru et al. 2017; Boro Saikia et al. 2018). See Sect. 4.3 for a search for periodic signals in other spectroscopic activity indicators. We also looked for soft X-ray and ultraviolet data of TOI-1235, but the star was not covered by any pointing (*XMM-Newton*, *Chandra*, *EUVE*), or was too faint and far from axis to be detected (*ROSAT*, *GALEX*). As an inactive member of the thin disk without further definitive evidence to support a very young or very old age, TOI-1235 is likely between 0.6 Ga (older than the Hyades) and 10 Ga (younger than low-metallicity, thick disk stars).

Table 3 summarizes the stellar properties of TOI-1235. We provide the most precise average values, their uncertainties, and corresponding reference.

4. Analysis and results

4.1. Limits on photometric contamination

We put limits to the dilution factor and to the presence of contaminant sources that can affect both photometric and radial-velocity measurements of TOI-1235. This is particularly relevant for the *TESS* photometry because of its large pixel size (~21 arcsec). The CARMENES and HARPS-N optical fiber apertures projected on the sky have, in contrast, sizes of only 1.5 arcsec and 1.0 arcsec, respectively, but the presence of a very close companion unresolved in all-sky imaging surveys from the ground and space could have a strong impact on our results.

First, we verified that the sources in the selection apertures in the *TESS* pixel file (TPF) did not affect the depth of the transits significantly. The TPFs shown in Fig. 2 were created with `tpfplotter`[6] (Aller et al. 2020). In particular, *Gaia* DR2 sources #2 and #3 in Sector 14, #4 in Sector 20, and #8 in Sector 21 have all G-band fluxes less than 0.5 % that of TOI-1235 (*Gaia* and the *TESS* photometric bands are very similar). Similar results were found for the apertures of the ground-based surveys ASAS-SN and NSVS.

For sub-arcsecond separations, we used our lucky-imaging AstraLux and speckle NESSI data sets described in Sect. 2.3 and illustrated by Fig. 3. We computed 5σ contrast curves as described in Lillo-Box et al. (2012) with the `astrasens` package[7] for AstraLux, and as in Livingston et al. (2018) for NESSI. From both data sets, we confirmed the absence of any close companion 4–6 mag fainter than TOI-1235, and derived an upper limit to the contamination of around 2 % between 0.15 arcsec and 1.5 arcsec (6.0–60 au if physically bound).

A further constraint came from the *Gaia* DR2 renormalized unit weight error (`RUWE`) value, which for TOI-1235 is 1.03, below the critical value of 1.40 that "indicates that a source is non-single or otherwise problematic for the astrometric solution" (Arenou et al. 2018; Lindegren et al. 2018). We also looked for wide common proper motion companions with similar *Gaia* DR2 parallax, as in Montes et al. (2018), and found none within 30 arcmin of our star. Following these results, we concluded that TOI-1235 is a single star, estimated the *TESS* and LCOGT dilution factors at $D = 1.0$ with Eq. 2 in Espinoza et al. (2019), and fixed this value for all our model fits in the next Sections.

4.2. Stellar rotational period from photometric data

The low activity levels of TOI-1235 probably imply a slow rotation. Empirically, the measured limit on rotational velocity ($v \sin i < 2\,{\rm km\,s^{-1}}$) places a lower limit on $P_{\rm rot}/\sin i > 15.7$ d. Although the actual inclination of the star is not known, the short-period transiting planet around such a low-mass stars hints towards a low obliquity (Winn et al. 2017), so that most probably $\sin i \sim 1$ and, therefore, $P_{\rm rot} \gtrsim 16$ d. On the other hand, from the $\log R'_{\rm HK}$-$P_{\rm rot}$ relation of Astudillo-Defru et al. (2017), TOI-1235 has a most likely $P_{\rm rot}$ of $27.8^{+2.0}_{-1.8}$ d.

To try to determine the actual rotational period of the star, we carried out different analyses of the available photometric data for TOI-1235. First, we employed the traditional periodogram analysis to search for significant peaks from the ASAS-SN g'- and V-band light curves. With the generalized Lomb-Scargle periodogram (GLS) of Zechmeister & Kürster (2009), we obtained a peak at 48.63 ± 0.08 d above the 10 % false-alarm probability (FAP) threshold for the combined light curve after subtracting an independent zero point from each band. We explored the time parameter space between 10 d and 1000 d. Since the ASAS-SN light curves contained a significant number (15 %) of outlying data points because of flares and poor signal-to-noise ratios that might bias the previous GLS analysis, we repeated the GLS anal-

---

[6] `https://github.com/jlillo/tpfplotter`

[7] `https://github.com/jlillo/astrasens`

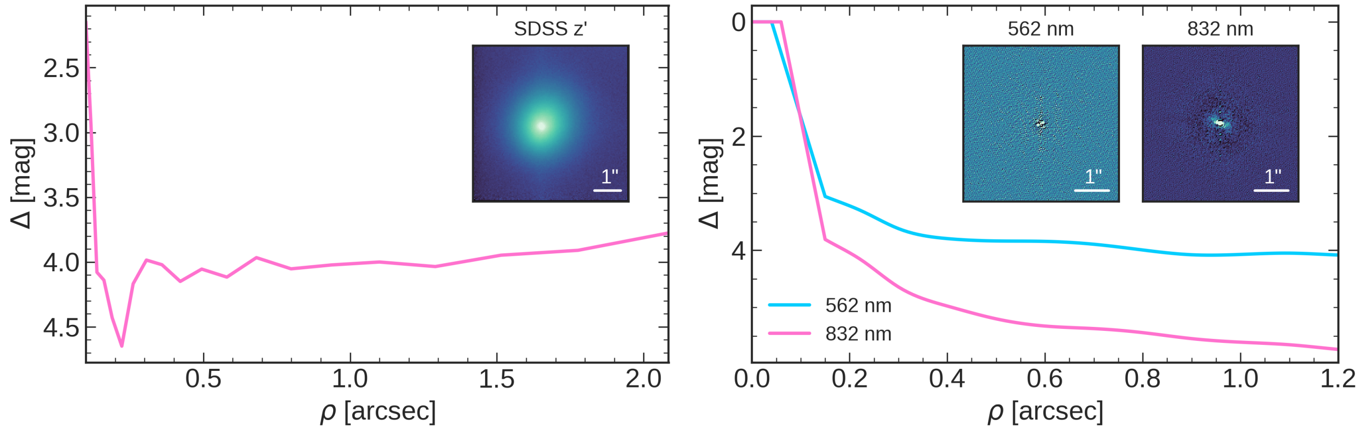

Fig. 3. Contrast curves (5σ) of TOI-1235 from AstraLux (*left*) and NESSI (*right*) observations. Inset images are $6.0 \times 6.0\,\mathrm{arcsec}^2$ stacked in z' band and $4.6 \times 4.6\,\mathrm{arcsec}^2$ reconstructed in 562 nm and 832 nm, respectively.

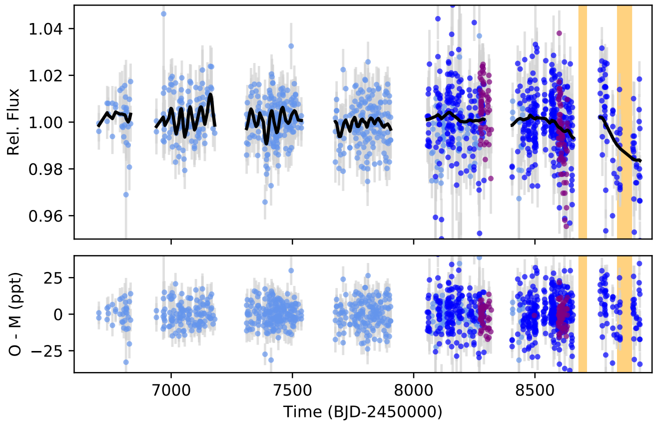

Fig. 4. ASAS-SN (V passband in light blue, g' passband in dark blue) and NSVS (purple) long-term photometric monitoring modeled with a quasi-periodic GP kernel defined as in Foreman-Mackey et al. (2017). The time span of the *TESS* observations is shown in gold.

ysis after removing these deviant data from the two light curves in two steps: we applied first a 2σ and then a 1σ clipping algorithm. The new GLS periodogram of the resulting combined g' and V data looked different to the one of the original ASAS-SN data, as there were no significant peaks in the studied parameter space. The highest peak near the 10 % FAP level was located, however, at a longer period of 136.9 ± 1.4 d. The amplitude of the "cleaned" ASAS-SN g'- and V-band light curve folded in phase with this long period was only 1.4 mmag.

Next, we used a more sophisticated model, fitting the ASAS-SN and NSVS photometry with a quasi-periodic Gaussian process (GP). In particular, we used the GP kernel introduced by Foreman-Mackey et al. (2017) of the form

$$k_{i,j}(\tau) = \frac{B}{2+C} e^{-\tau/L} \left[\cos\left(\frac{2\pi\tau}{P_{\mathrm{rot}}}\right) + (1+C) \right] \quad ,$$

where $\tau = |t_i - t_j|$ is the time-lag, B and C define the amplitude of the GP, L is a timescale for the amplitude-modulation of the GP, and P_{rot} is the period of the quasi-periodic modulations. For the fit, we considered that each instrument and pass band could have different values of B and C, while L and P_{rot} were left as common parameters. We considered wide uninformative priors for B, C (log-uniform between 10^{-3} ppm and 10^8 ppm), L (log-uniform between 10^2 d and 10^8 d), P_{rot} (uniform between 10 d and 300 d), and instrumental jitter (log-uniform between 10 ppm and 10^6 ppm). The fit was performed using `juliet` (Espinoza et al. 2019, see next section for a full description of the algorithm), and the resulting fit is presented in Fig. 4. The rotational period from the quasi-periodic GP analysis was found to be $P_{\mathrm{rot}} = 41.2^{+1.1}_{-1.2}$ d, with an amplitude of about 10 mmag during the time of highest stellar variability. This period is close to the one-year alias of the period previously obtained via the GLS analysis of the raw ASAS-SN data.

Finally, we took advantage of the *TESS* observations of TOI-1235 in three sectors spanning almost 210 d. We analyzed the light curve described in Sect. 2.1 and two light curves obtained from an optimized aperture (González-Cuesta et al. in prep.), in which we selected pixels with integrated flux above thresholds of $10\,\mathrm{e}^-\,\mathrm{s}^{-1}$ and $20\,\mathrm{e}^-\,\mathrm{s}^{-1}$, respectively. We then corrected the light curves for outliers and jumps, filled the gaps, concatenated the three sectors following García et al. (2011, 2014b), and removed the transits to make sure that they were not biasing the results. Finally, we applied our rotation pipeline (Mathur et al. 2010; García et al. 2014a; Santos et al. 2019) with three different methods to look for a periodicity in the data: time-frequency analysis (Torrence & Compo 1998), autocorrelation function (McQuillan et al. 2014), and composite spectrum (Ceillier et al. 2017). While different combinations of methods and light curves generally yielded somewhat different periodicities, signals in the range 32–42 d were present in the time-frequency and composite spectrum analysis of the last two sectors. However, the significance of the peaks was slightly below our criteria for establishing a reliable period (Ceillier et al. 2017).

To sum up, the GLS periodogram of the raw ASAS-SN data, the quasi-periodic GP modeling of the combined ASAS-SN and NSVS data, and the s-BGLS analysis of the spectroscopic data (see Sect. 4.3) all point towards a stellar origin of the ~ 40 d photometric signal, which suggest that this value could be the true rotation period of TOI-1235.

4.3. *Signals in spectroscopic data*

We searched for periodic signals in the combined CARMENES VIS and HARPS-N radial velocity data by computing GLS periodograms, as illustrated by Fig. 5. A signal corresponding to the transits in the *TESS* light curve was significantly detected

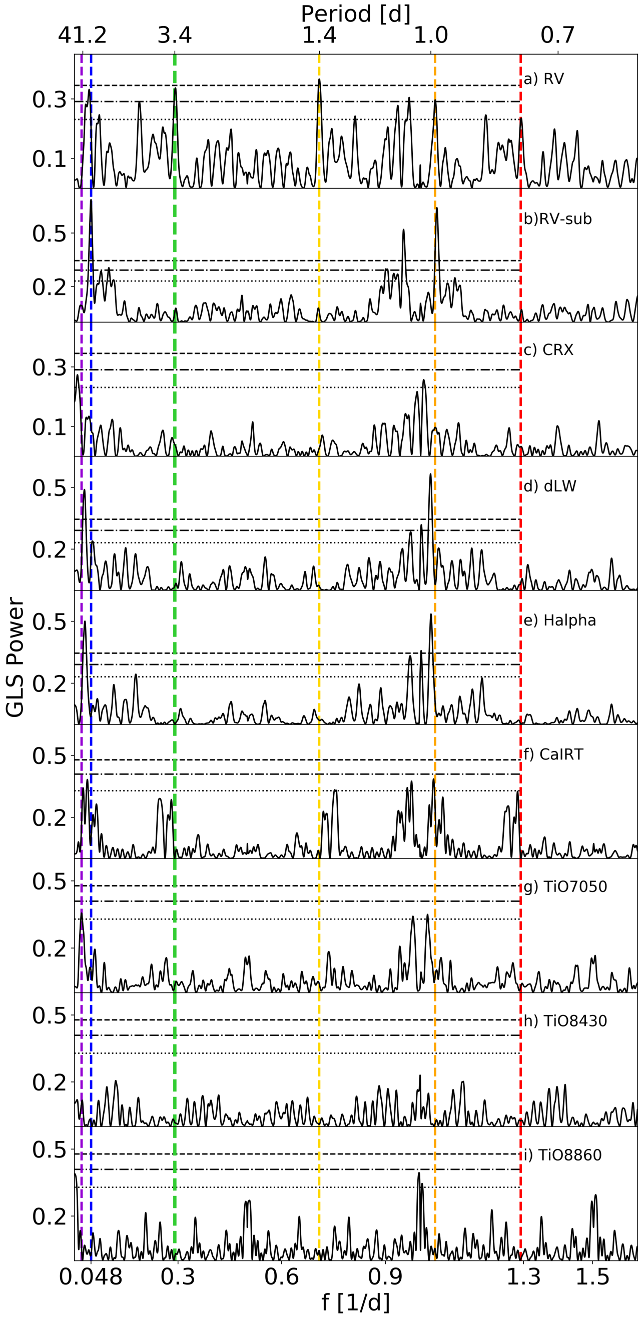

Fig. 5. GLS periodograms of: (*a*) combined radial velocities from CARMENES VIS and HARPS-N, (*b*) RV residuals after subtracting the planet signal, (*c*-*e*) combined CRX, dLW, and Hα index from CARMENES VIS and HARPS-N, and (*f*-*i*) Ca IRT, TiO7050, TiO8430, and TiO8860 indices from CARMENES only. In all panels the vertical dashed lines indicate the periods of 3.44 d (thick green, planet), 41.2 d (violet, $P_{\rm rot}$ from the quasi-periodic GP analysis of the combined ASAS-SN and NSVS photometry), 20.6 d (blue, stellar activity), and their aliases (yellow, orange, and red). The horizontal lines mark the theoretical FAP levels of 0.1 % (dotted), 1 % (dash-dotted), and 10 % (dashed).

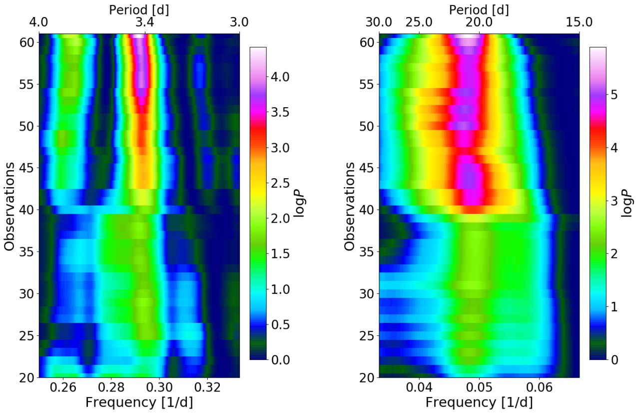

Fig. 6. Evolution of the s-BGLS periodogram of the CARMENES and HARPS-N RV data of TOI-1235 around the 3.44 d signal of the transiting planet (*left*) and around the 20.6 d activity signal after subtracting the planet signal (*right*). The number of data points included in the computation of the periodogram increases from bottom to top.

in the RVs at $P_{\rm b}$ = 3.44 d (FAP ~1 %; panel *a*). However, we also found an additional signal at $P \approx 20.6$ d, at about half the most likely stellar rotation period, and its aliases at 1.4 d, 1.0 d, and 0.77 d. After removing the planetary signal, the 20.6 d signal and its aliases still remained with a FAP $\gtrsim$ 0.1 % (panel *b*).

To understand the origin of this signal, we searched for additional peaks in the periodograms of the activity indicators CRX, dLW, and Hα derived from the individual CARMENES and HARPS-N spectra (panels *c*-*e*), and Ca IRTa (panel *f*), and the titanium oxide indices that quantify the strengths of the TiO γ, ϵ, and δ absorption band heads at 7050 Å, 8430 Å, and 8860 Å (panels *g*-*i*), respectively, from the CARMENES spectra only (Zechmeister et al. 2018; Schöfer et al. 2019). The activity indices and their uncertainties are listed in Table A.2. Except for daily aliases, the highest peaks in the dLW, Hα, Ca IRTa, and TiO7050 periodograms are at around $P \approx$ 32–47 d, which adds further credence to $P_{\rm rot} \sim 40$ d as inferred in Section 4.2. All these indicators track different features in the stellar atmosphere, and our spectra cover only slightly more than two periods, so it is plausible that they do not yield exactly the same periods. We also detected the 20.6 d signal in the dLW series, which supports the notion that this signal is also related to stellar activity. As expected for an early-type M dwarf, the TiO8430 and TiO8860 indices showed no significant signals.

We used the stacked Bayesian generalized Lomb-Scargle periodogram (s-BGLS; Mortier et al. 2015) with the normalization of Mortier & Collier Cameron (2017) to verify whether the 20.6 d signal was coherent over the whole observational time baseline of CARMENES and HARPS-N. In Fig. 6, we display s-BGLS periodograms of the raw RV data around 3.44 d, and of the RV data, after subtracting a sinusoid at the transiting planet period, around the 20.6 d signal. This signal showed a first probability maximum after around 44 observations (BJD ~ 2458663) and thereafter decreased for some time. Such incoherence is characteristic of a non-planetary origin of the signal (Mortier & Collier Cameron 2017). The s-BGLS of the 3.44 d signal, on the other hand, showed a monotonically increasing probability, as expected for a Keplerian signal.

Lastly, we measured Pearson's r, Student's t, and Fisher's z correlation coefficients between the temporal series of RV and the activity indicators CRX, dLW, Hα, Ca IRTa, TIO7050, and $S_{\rm MWO}$, and we did not see any intrinsic correlation between RV and activity as in Gan et al. (2020). In particular, we determined absolute values of r and z below 0.006 and of t above 0.7, respectively, for all relations except for RV vs. dLW, which was in any case weakly anti-correlated.

4.4. Joint fit

To obtain precise parameters of the TOI-1235 system, we performed a joint analysis of the *TESS* and LCOGT photometry and CARMENES VIS and HARPS-N RV data using `juliet`. We did not use CARMENES NIR data for the analysis because the expected radial-velocity amplitude of the planet is lower than the median radial precision obtained in the NIR channel (Bauer et al. 2020), nor the TJO data because of an observational gap in the middle of the transit. For the radial-velocity modelling, the model we selected in our joint fit analysis was one composed of a circular Keplerian orbit for the transiting planet plus a quasi-periodic GP which we used to model the 20.6 d signal observed in the radial-velocities and already discussed in previous sections. However, we also computed models of a circular orbit, an eccentric orbit, a circular orbit plus a sinusoid, an eccentric orbit plus a sinusoid, an eccentric orbit plus a GP, and two circular orbits. The two "best" models, judged by their log-evidences, were a two-planet model and the one using a GP to fit the 20.6 d signal. However, the difference between their log-evidences was $\Delta \ln \mathcal{Z} < 2$, which made the two models indistinguishable if they were equally likely a priori. Actually, both models gave almost identical constraints on the properties of the transiting exoplanet. The analyses on the activity indices and photometric data, however, gave a larger prior weight to the stellar activity model and, thus, we decided to use a GP — which is typically better at modelling stellar activity than a simple sinusoid — as our final model to account for the 20.6-day signal. In our analysis we used the exp-sine-squared kernel for the GP, which is a very common kernel to model stellar activity signatures in the literature (see, e.g., Nava et al. 2020, and references therein), and which is of the form

$$k_{i,j}(\tau) = \sigma_{\rm GP}^2 \exp\left(-\alpha\tau^2 - \Gamma \sin^2\left[\frac{\pi\tau}{P_{\rm rot}}\right]\right).$$

For the transit modeling, `juliet` uses the `batman` package (Kreidberg 2015). To parameterize the limb-darkening effect in the *TESS* photometry, we employed the efficient, uninformative sampling scheme of Kipping (2013) and a quadratic law. We used a common set of limb-darkening coefficients across the three *TESS* sectors. In the LCOGT lightcurve analysis, we instead used a linear law to parameterize the limb-darkening effect, as a more complex law was not warranted given the precision of the data, as explained by Espinoza & Jordán (2016). We used the Espinoza (2018) parameterization to explore the full physically plausible parameter space for the planet-to-star radius ratio, $R_p/R_\star$, and impact parameter, b. Finally, we used a white-noise-only fit for the *TESS* photometry, as an analysis using a GP on the photometry returned a log-evidence that was indistinguishable from the one of a white-noise model. For the LCOGT photometry, on the other hand, we used a linear model to detrend the data, with airmass and pixel position of the target as regressors. The priors used for our joint fit are presented in Table A.1.

As illustrated by the posterior parameters of our joint fit presented in Table 4 and the resulting RV model presented in Fig. 7, the period of the quasi-periodic GP component of the RV part of our model, $P_{\rm rot;GP,RV}$, is about 20.9 d, in agreement with the signal observed in the GLS periodogram of the RVs (Fig. 5). This is almost exactly half the period derived from the long-term photometric monitoring discussed in previous Sections, which means that a rotating spotted stellar surface is the most plausible cause of these variations. Consequently, we performed joint fits using the period observed in the photometry of $P_{\rm rot} = 41.2^{+1.2}_{-1.5}$ d as a prior, and the results were almost identical regarding the properties of the transiting planet to the ones presented in Table 4. Therefore, our model marginalized properly over the possible different scenarios on the stellar surface in terms of stellar activ-

Table 4. Posterior parameters of the `juliet` joint fit for TOI-1235 b.

Parameter[a]	TOI-1235 b
Stellar parameters	
$\rho_\star$ (g cm^{-3})	$3.74^{+0.30}_{-0.31}$
Planet parameters	
P (d)	$3.444717^{+0.000040}_{-0.000042}$
t_0 (BJD)	$2458683.6155^{+0.0017}_{-0.0015}$
$a/R_\star$	$13.29^{+0.34}_{-0.38}$
$p = R_{\rm p}/R_\star$	$0.02508^{+0.00084}_{-0.00085}$
$b = (a/R_\star)\cos i_{\rm p}$	$0.25^{+0.12}_{-0.14}$
$i_{\rm p}$ (deg)	$88.90^{+0.62}_{-0.57}$
r_1	$0.500^{+0.081}_{-0.097}$
r_2	$0.02506^{+0.00083}_{-0.00085}$
K (m s^{-1})	$3.40^{+0.35}_{-0.34}$
Photometry parameters	
$M_{\rm TESS,S14}$ (10^{-6})	$-31.0^{+8.5}_{-8.3}$
$M_{\rm TESS,S20}$ (10^{-6})	$-17.0^{+8.3}_{-8.2}$
$M_{\rm TESS,S21}$ (10^{-6})	$-24.0^{+8.0}_{-8.0}$
$\sigma_{\rm TESS,S14}$ (ppm)	$1.9^{+10.5}_{-1.6}$
$\sigma_{\rm TESS,S20}$ (ppm)	$1.9^{+8.2}_{-1.6}$
$\sigma_{\rm TESS,S21}$ (ppm)	$1.5^{+7.8}_{-1.3}$
$q_{1,\rm TESS}$	$0.42^{+0.32}_{-0.25}$
$q_{2,\rm TESS}$	$0.31^{+0.30}_{-0.20}$
$M_{\rm LCO}$ (10^{-6})	-257^{+84}_{-86}
$\sigma_{\rm LCO}$ (ppm)	970^{+82}_{-83}
$q_{1,\rm LCO}$	$0.49^{+0.30}_{-0.30}$
$\theta_{0,\rm LCO}$ (10^{-6})	-10^{+11}_{-11}
$\theta_{1,\rm LCO}$ (10^{-6})	-49^{+11}_{-11}
RV parameters	
$\gamma_{\rm CARMENES}$ (m s^{-1})	$-3.0^{+4.6}_{-4.3}$
$\sigma_{\rm CARMENES}$ (m s^{-1})	$0.17^{+0.61}_{-0.14}$
$\gamma_{\rm HARPS-N}$ (m s^{-1})	$3.8^{+4.6}_{-4.2}$
$\sigma_{\rm HARPS-N}$ (m s^{-1})	$1.29^{+0.43}_{-0.37}$
GP hyperparameters	
$\sigma_{\rm GP,RV}$ (m s^{-1})	$12.3^{+17.9}_{-6.3}$
$\alpha_{\rm GP,RV}$ (10^{-6} d^{-2})	74^{+127}_{-50}
$\Gamma_{\rm GP,RV}$ (d^{-2})	$0.084^{+0.251}_{-0.068}$
$P_{\rm rot;GP,RV}$ (d)	$20.93^{+0.56}_{-0.52}$

Notes. (a) Priors and descriptions for each parameter are in Table A.1. Error bars denote the 68 % posterior credibility intervals.

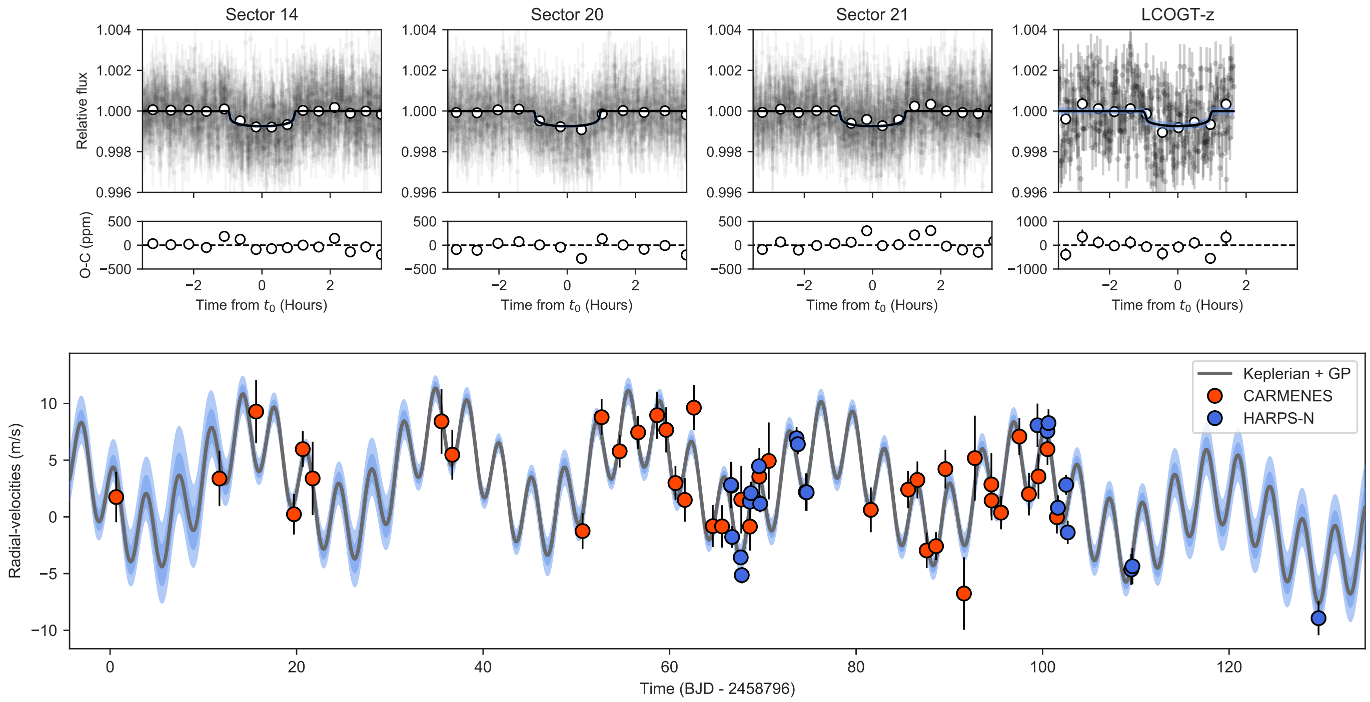

Fig. 7. Joint fit results. *Top panels:* phase-folded light curves of *TESS*, Sectors 14, 20, and 21, and LCOGT, from left to right, and their residuals. White circles are binned data (shown only for reference; data used to fit the model were the unbinned points), black curves are the best-fit models, and blue areas are the 68 % credibility bands. *Bottom panel:* CARMENES (orange) and HARPS-N (blue) radial velocities. The grey curve is the median best-fit `juliet` model, and the light and dark blue areas are its 68 % and 95 % credibility bands.

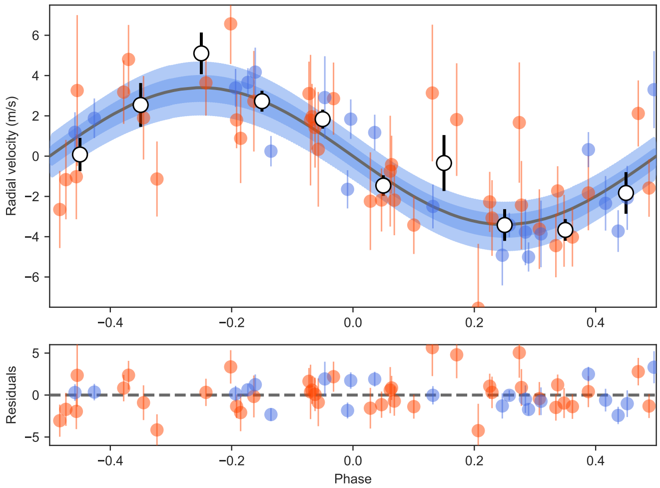

Fig. 8. Phase-folded RVs for TOI-1235 with the GP component removed. Orange circles are CARMENES data, blue circles are HARPS-N data, white points are binned data for reference. Grey curve is the median best-fit `juliet` model, and the light and dark blue areas are its 68 % and 95 % credibility bands.

Table 5. Derived planetary parameters for TOI-1235 b.

Parameter[a]	TOI-1235 b
Derived transit parameters	
u_1[b]	$0.38^{+0.30}_{-0.24}$
u_2[b]	$0.22^{+0.35}_{-0.32}$
t_T (h)	$2.094^{+0.126}_{-0.086}$
Derived physical parameters	
M_p ($M_\oplus$)	$5.90^{+0.62}_{-0.61}$
R_p ($R_\oplus$)	$1.694^{+0.080}_{-0.077}$
ρ_p (g cm^{-3})	$6.7^{+1.3}_{-1.1}$
g_p (m s^{-2})	$20.1^{+3.0}_{-2.7}$
a_p (au)	$0.03826^{+0.00048}_{-0.00049}$
T_eq (K)[c]	775^{+13}_{-13}
S ($S_\oplus$)	$60.3^{+1.6}_{-1.5}$

Notes. [a] Parameters obtained with the posterior values from Table 4, t_T=Transit duration, from first contact to fourth contact. Error bars denote the 68 % posterior credibility intervals. [b] Derived from the *TESS* light curve. [c] The equilibrium temperature was calculated assuming zero Bond albedo.

ity. As shown in Fig. 8 and Table 4, we attained a 10σ detection of the planetary RV semi-amplitude.

To sum up, the TOI-1235 system consists of a relatively inactive early M dwarf with at least one super-Earth-like planet, namely TOI-1235 b (see Table 5), with a mass of $M_\mathrm{p} = 5.9^{+0.6}_{-0.6}\,M_\oplus$ and radius of $R_\mathrm{p} = 1.69^{+0.08}_{-0.08}\,R_\oplus$ in a circular orbit with a period of 3.44 d. We also derived a bulk density of $\rho_\mathrm{p} = 6.7^{+1.3}_{-1.1}$ g cm^{-3} and an equilibrium temperature, assuming a zero albedo, of $T_\mathrm{eq} = 776 \pm 13$ K, slightly hotter than the mean surface temperature of Venus.

4.5. Search for transit depth and time variations

TESS observed TOI-1235 in three sectors and covered 19 transits of TOI-1235 b. This allowed us to assess the presence of transit timing variations (TTVs) and transit depth variations. We carried out a search for TTVs using the `batman` package and fitted each transit individually, only leaving transit times and transit depth as free parameters, and fixing the rest of the parameters to the values obtained in the joint analysis in Sect. 4.4. The best-fit parameters and associated uncertainties in our fitting procedure were derived using a Markov chain Monte Carlo analysis implemented in the `emcee` python package (Foreman-Mackey et al. 2013). We found a hint of periodic TTV signal with a semi-amplitude of about 4 min. Using the GLS of the observed TTV signal, we found that the observed TTVs had a periodicity of 25.3±0.2 d, which could indicate the presence of a second non-transiting planet in the system (Holman & Murray 2005). However, a TTV signal with this amplitude could also be easily generated by the stellar activity (e.g., Oshagh et al. 2013), and the period was consistent with our previous analyses of the stellar rotation. We also looked for trends in the derived transit depths, and found that individual depths agreed within 1σ with that derived from the combined analysis.

5. Discussion

Our 61 RV measurements yield a planetary mass for TOI-1235 b with an uncertainty of about 10 %, and the *TESS* and LCOGT light curves constrain the planetary radius at a level of about 5 % uncertainty. Therefore, TOI-1235 b belongs to the selected group of terrestrial planets with a well-determined bulk density. The population with measurements better than 30 % is shown in the mass-radius diagram of Fig. 9. The comparison of TOI-1235 b with theoretical models of Zeng et al. (2016, 2019) is consistent with a rocky, $MgSiO_3$-dominated composition with a bulk density slightly higher than Earth's, classifying it as a super-Earth planet.

Also using the mass and radius relationships from Zeng et al. (2016), the best fit results in an iron core mass fraction of ~12 %, but the planet is also consistent, within 1σ, with an Earth-like bulk composition. Furthermore, using `Hardcore` (Suissa et al. 2018) and our R and M, the marginal core ratio fraction, $\mathrm{CRF}_{\mathrm{marg}}$, is 0.53±0.20, similar to the Earth's true CRF value of 0.55.

Like many other transiting terrestrial and sub-Neptune planets, TOI-1235 b is on a fairly irradiated orbit and so may have been strongly sculpted by extreme atmospheric escape due to XUV-driven photo-evaporation (e.g., López & Fortney 2013; Owen & Wu 2013) or core-powered mass loss (e.g., Wu 2019; Gupta & Schlichting 2020). Reaching the required binding energy makes that explanation difficult for TOI-1235 b, but using the escape scaling relations from López & Fortney (2013) we find that this planet lies right at the boundary of where escape evolution is likely to play a significant role in removing primordial H/He gaseous envelopes.

As described in Sect. 1 and illustrated by the insolation-radius diagram in Fig. 9, the growing exoplanet statistics has revealed a gap in the radius distribution of planets slightly larger than Earth (Fulton et al. 2017). Rocky super-Earth planets of up to $\sim 1.5\,R_\oplus$ are relatively common, as are gaseous mini-Neptunes in the range of 2–$4\,R_\oplus$, but only a few planets have been detected with a radius inside this gap (Gandolfi et al. 2019). Using the location of the radius valley as determined by Van Eylen et al. (2018), i.e., $\log R = m \log P + a$ with $m = -0.09^{+0.02}_{-0.04}$ and $a = 0.37^{+0.04}_{-0.02}$, we determine the predicted location of the radius valley at the orbital period of TOI-1235 b. We find that for $P = 3.44$ d, the radius valley is located at $R = 2.1 \pm 0.2\,R_\oplus$. Therefore, and according to that definition, TOI-1235 b, which has a radius $R = 1.69^{+0.08}_{-0.07}\,R_\oplus$, would be located near the lower edge of the radius valley. Indeed, its rocky composition is consistent with the planet having lost its atmosphere, as expected for planets below the radius valley (e.g. Owen & Wu 2013).

However, the location of the radius gap as determined by Van Eylen et al. (2018) was based on F, G, and K-type stars, whereas TOI-1235 b orbits an M dwarf star. Whether these same boundaries apply to M dwarfs (and whether the gap actually exists for planets around M dwarfs) has been the subject of several recent studies (Zeng et al. 2017; Fulton & Petigura 2018; Hirano et al. 2018). Following Zeng et al. (2017), for example, which used all of the *Kepler* planet candidates, the radius and stellar irradiation level of TOI-1235 b puts it exactly on the gap for early M dwarfs (located at about $1.7\,R_\oplus$ for an irradiation of $60\,S_\oplus$ in that work). On the other hand, when extrapolating from the sample of Fulton & Petigura (2018), which focused on F, G and K-type stars with precise stellar parameters and that host validated *Kepler* exoplanets, one reaches a similar conclusion. Finally, using the sample of Hirano et al. (2018), which focused only on low-mass stars hosting validated small planets unveiled by K2 and *Kepler*, one would locate TOI-1235 b on the gap, but the data in that sample (arguably better curated for a proper comparison with the stellar properties of TOI-1235) was unable to track a proper stellar irradiation versus radius dependance of the gap. Therefore, our measurements of the bulk composition of TOI-1235 b, consistent with the planet having lost its atmosphere, puts a strong constraint on any interpretation regarding the radius gap for M dwarfs at the irradiation levels received by TOI-1235 b. If atmospheric loss is indeed the correct physical interpretation for the radius gap, and it applies to M dwarfs at the period/stellar irradiation level of TOI-1235 b, the gap for early-type M dwarfs has to be either at or above $1.7\,R_\oplus$.

6. Conclusions

In this paper we confirmed that TOI-1235 b is a transiting super-Earth planet around an M0.5 V star, observed in Sectors 14, 20, and 21 of the *TESS* mission. We collected CARMENES and HARPS-N spectroscopic data, from which we confirmed the planetary nature of the transit signal detected by *TESS*. In addition, we obtained LCOGT photometric data during one transit event, and lucky imaging and speckle observations. From the joint analysis of all the data, we derived the following parameters for TOI-1235 b: a mass of $M_p = 5.9 \pm 0.6\,M_\oplus$, a radius of $R_p = 1.69 \pm 0.08\,R_\oplus$, and a density of $\rho_{\mathrm{p}} = 6.7^{+1.7}_{-1.1}\,\mathrm{g\,cm^{-3}}$.

Comparing the physical properties of TOI-1235 b with compositional models reveals the planet to be a rocky super-Earth, with a bulk density only slightly higher than Earth's. Although there is still debate on the literature as to the location (and existence) of a radius gap for exoplanets around M-dwarfs, the radius and irradiation level of TOI-1235 b puts it at the radius gap according to various suggestions of its location in the literature for these small, low mass stars. If the gap indeed exists for M-dwarfs, the bulk properties of TOI-1235 b, which makes it consistent with having lots its atmosphere, constrain the gap to be at or above the planetary radius of TOI-1235 b, i.e., $\sim 1.7 R_\oplus$ at its irradiation level ($\sim 60 S_\oplus$). These findings helps to better constrain the dependence of the gap location on the stellar type and irradiation, and thus to understand its origin. Finally, the brightness of TOI-1235 ($V \approx 11.5$ mag) makes this planet an accessible

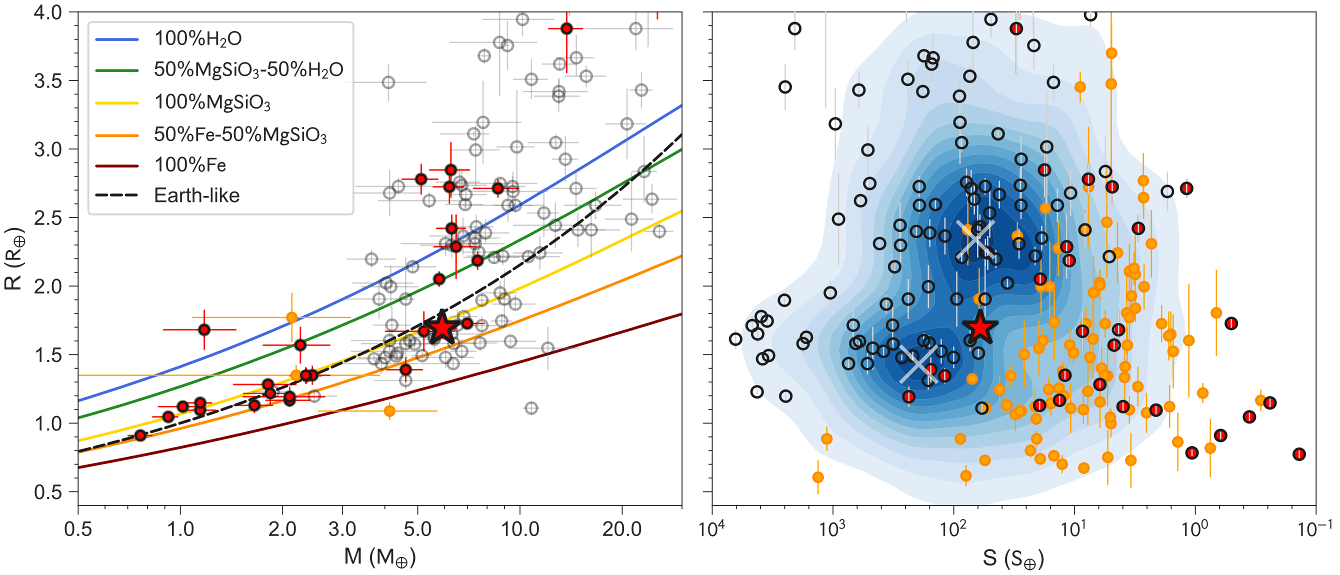

Fig. 9. Mass-radius (*left*) and insolation-radius (*right*) diagrams in Earth units. In the two panels, open circles are transiting planets around F-, G-, and K-type stars with mass and radius measurement better than 30 % from the TEPCat database of well-characterized planets (Southworth 2011), filled red circles are planets around M dwarfs with mass and radius measurement, planets around M dwarfs with mass determinations worse than 30 % or without mass constraints at all (*right* panel only), and the red star is TOI-1235 b, which has radius and mass determined with accuracies of 5 % and 10 %, respectively. In the *left* panel, the color lines are the theoretical *R*-*M* models of Zeng et al. (2016), and the three planets with mass determination worse than 30 % are K2–3 b, BD–17 588A b, and LHS 1815 b (Almenara et al. 2015; Winters et al. 2019; Gan et al. 2020). In the *right* panel, we plot the *R*-*S* point density of all the known confirmed transiting planets with contours, and mini-Neptunes and super-Earths density maxima with white crosses. The M dwarf without mass determination in the radius gap is K2–104 b (Mann et al. 2017), a planet around an active star in the Praesepe cluster fainter by 5 mag in *V* than TOI-1235.

and very interesting object for further studies of planet formation and atmospheric evolution.

Acknowledgements. CARMENES is an instrument for the Centro Astronómico Hispano-Alemán de Calar Alto (CAHA, Almería, Spain). CARMENES is funded by the German Max-Planck-Gesellschaft (MPG), the Spanish Consejo Superior de Investigaciones Científicas (CSIC), the European Union through FEDER/ERF FICTS-2011-02 funds, and the members of the CARMENES Consortium (Max-Planck-Institut für Astronomie, Instituto de Astrofísica de Andalucía, Landessternwarte Königstuhl, Institut de Ciències de l'Espai, Institut für Astrophysik Göttingen, Universidad Complutense de Madrid, Thüringer Landessternwarte Tautenburg, Instituto de Astrofísica de Canarias, Hamburger Sternwarte, Centro de Astrobiología and Centro Astronómico Hispano-Alemán), with additional contributions by the Spanish Ministry of Economy, the German Science Foundation through the Major Research Instrumentation Programme and DFG Research Unit FOR2544 "Blue Planets around Red Stars", the Klaus Tschira Stiftung, the states of Baden-Württemberg and Niedersachsen, and by the Junta de Andalucía. We acknowledge the use of public TESS Alert data from pipelines at the TESS Science Office and at the TESS Science Processing Operations Center. This research has made use of the Exoplanet Follow-up Observation Program website, which is operated by the California Institute of Technology, under contract with the National Aeronautics and Space Administration under the Exoplanet Exploration Program. Resources supporting this work were provided by the NASA High-End Computing (HEC) Program through the NASA Advanced Supercomputing (NAS) Division at Ames Research Center for the production of the SPOC data products. We acknowledge financial support from the European Research Council under the Horizon 2020 Framework Program via the ERC Advanced Grant Origins 83 24 28, the Deutsche Forschungsgemeinschaft through projects RE 281/32-1, RE 1664/14-1, RE 2694/4-1, and RA714/14-1, PA525/18-1, PA525/19-1 within the Schwerpunkt SPP 1992, the Agencia Estatal de Investigación of the Ministerio de Ciencia, Innovación y Universidades and the European FEDER/ERF funds through projects PGC2018-098153-B-C31, ESP2016-80435-C2-1-R, ESP2016-80435-C2-2-R, AYA2016-79425-C3-1/2/3-P, AYA2015-69350-C3-2-P, RYC-2015-17697, and BES-2017-082610, the Centre of Excellence "Severo Ochoa" and "María de Maeztu" awards to the Instituto de Astrofísica de Canarias (SEV-2015-0548), Instituto de Astrofísica de Andalucía (SEV-2017-0709), and Centro de Astrobiología (MDM-2017-0737), the European Union's Horizon 2020 research and innovation program under the Marie Skłodowska-Curie grant 713673, the Centre national d'études spatiales through grants PLATO and GOLF, the Czech Academy of Sciences through grant LTT20015, NASA through grants NNX17AF27G and NNX17AG24G, JSPS KAKENHI through grants JP18H01265 and JP18H05439, JST PRESTO through grant JPMJPR1775, the Fundación Bancaria "la Caixa" through grant INPhINIT LCF/BQ/IN17/11620033, and the Generalitat de Catalunya/CERCA programme. NESSI was funded by the NASA Exoplanet Exploration Program and the NASA Ames Research Center and built at the Ames Research Center. The authors are honored to be permitted to conduct observations on Iolkam Du'ag (Kitt Peak), a mountain within the Tohono O'odham Nation with particular significance to the Tohono O'odham people. This work made use of observations from the LCOGT network and the following software: `astrasens`, `AstroImageJ`, `Banzai`, `batman`, `CARACAL`, `emcee`, `juliet`, `SERVAL`, `TESS Transit Finder`, `tpfplotter`, `Yabi`, and the python packages `astropy`, `lightkurve`, `matplotlib`, and `numpy`. We thank the SuperWASP team and J. Sanz-Forcada for sharing unpublished information with us. Special thanks to Ismael Pessa for all their support through this work.

References

Aller, A., Lillo-Box, J., Jones, D., Miranda, L. F., & Barceló Forteza, S. 2020, A&A, 635, A128
Almenara, J. M., Astudillo-Defru, N., Bonfils, X., et al. 2015, A&A, 581, L7
Alonso-Floriano, F. J., Morales, J. C., Caballero, J. A., et al. 2015, A&A, 577, A128
Arenou, F., Luri, X., Babusiaux, C., et al. 2018, A&A, 616, A17
Astudillo-Defru, N., Delfosse, X., Bonfils, X., et al. 2017, A&A, 600, A13
Bakos, G., Noyes, R. W., Kovács, G., et al. 2004, PASP, 116, 266
Batalha, N. M., Rowe, J. F., Bryson, S. T., et al. 2013, ApJS, 204, 24
Bauer, F. F., Zechmeister, M., Kaminski, A., & et al. 2020, A&A, subm.
Bayo, A., Rodrigo, C., Barrado Y Navascués, D., et al. 2008, A&A, 492, 277
Berger, T. A., Huber, D., Gaidos, E., & van Saders, J. L. 2018, ApJ, 866, 99
Bonfils, X., Delfosse, X., Udry, S., et al. 2013, A&A, 549, A109
Boro Saikia, S., Marvin, C. J., Jeffers, S. V., et al. 2018, A&A, 616, A108
Borucki, W. J. 2016, Reports on Progress in Physics, 79, 036901
Borucki, W. J., Koch, D., Basri, G., et al. 2010, Science, 327, 977
Brown, T. M., Baliber, N., Bianco, F. B., et al. 2013, Publications of the Astronomical Society of the Pacific, 125, 1031

Ceillier, T., Tayar, J., Mathur, S., et al. 2017, A&A, 605, A111

Chabrier, G. 2003, PASP, 115, 763

Chen, H. & Rogers, L. A. 2016, ApJ, 831, 180

Cifuentes, C., Caballero, J. A., Cortés-Contreras, M., & et al. 2020, A&A, subm.

Collins, K. A., Kielkopf, J. F., Stassun, K. G., & Hessman, F. V. 2017, AJ, 153, 77

Cosentino, R., Lovis, C., Pepe, F., et al. 2012, Society of Photo-Optical Instrumentation Engineers (SPIE) Conference Series, Vol. 8446, Harps-N: the new planet hunter at TNG, 84461V

Crossfield, I. J. M., Waalkes, W., Newton, E. R., et al. 2019, ApJ, 883, L16

Cutri, R. M. & et al. 2014, VizieR Online Data Catalog, II/328

Díez Alonso, E., Caballero, J. A., Montes, D., et al. 2019, A&A, 621, A126

Drake, A. J., Djorgovski, S. G., Mahabal, A., et al. 2009, ApJ, 696, 870

Dressing, C. D. & Charbonneau, D. 2015, ApJ, 807, 45

Espinoza, N. 2018, Research Notes of the American Astronomical Society, 2, 209

Espinoza, N., Brahm, R., Henning, T., et al. 2020, MNRAS, 491, 2982

Espinoza, N. & Jordán, A. 2016, MNRAS, 457, 3573

Espinoza, N., Kossakowski, D., & Brahm, R. 2019, MNRAS, 490, 2262

Esposito, M., Armstrong, D. J., Gandolfi, D., et al. 2019, A&A, 623, A165

Foreman-Mackey, D., Agol, E., Ambikasaran, S., & Angus, R. 2017, celerite: Scalable 1D Gaussian Processes in C++, Python, and Julia

Foreman-Mackey, D., Hogg, D. W., Lang, D., & Goodman, J. 2013, PASP, 125, 306

Frith, J., Pinfield, D. J., Jones, H. R. A., et al. 2013, MNRAS, 435, 2161

Fulton, B. J. & Petigura, E. A. 2018, AJ, 156, 264

Fulton, B. J., Petigura, E. A., Howard, A. W., et al. 2017, AJ, 154, 109

Gagné, J., Mamajek, E. E., Malo, L., et al. 2018, ApJ, 856, 23

Gaia Collaboration, Brown, A. G. A., Vallenari, A., et al. 2018, A&A, 616, A1

Gaidos, E., Mann, A. W., Kraus, A. L., & Ireland, M. 2016, MNRAS, 457, 2877

Gaidos, E., Mann, A. W., Lépine, S., et al. 2014, MNRAS, 443, 2561

Gan, T., Shporer, A., Livingston, J. H., et al. 2020, AJ, 159, 160

Gandolfi, D., Barragán, O., Livingston, J. H., et al. 2018, A&A, 619, L10

Gandolfi, D., Fossati, L., Livingston, J. H., et al. 2019, ApJ, 876, L24

García, R. A. & Ballot, J. 2019, Living Reviews in Solar Physics, 16, 4

García, R. A., Ceillier, T., Salabert, D., et al. 2014a, A&A, 572, A34

García, R. A., Hekker, S., Stello, D., et al. 2011, MNRAS, 414, L6

García, R. A., Mathur, S., Pires, S., et al. 2014b, A&A, 568, A10

Gilbert, E. A., Barclay, T., Schlieder, J. E., et al. 2020, arXiv e-prints, arXiv:2001.00952

Ginzburg, S., Schlichting, H. E., & Sari, R. 2016, ApJ, 825, 29

Ginzburg, S., Schlichting, H. E., & Sari, R. 2018, MNRAS, 476, 759

Günther, M. N., Pozuelos, F. J., Dittmann, J. A., et al. 2019, Nature Astronomy, 3, 1099

Gupta, A. & Schlichting, H. E. 2019, MNRAS, 487, 24

Gupta, A. & Schlichting, H. E. 2020, MNRAS, 493, 792

Heinze, A. N., Tonry, J. L., Denneau, L., et al. 2018, AJ, 156, 241

Henry, T. J., Jao, W.-C., Subasavage, J. P., et al. 2006, AJ, 132, 2360

Hirano, T., Dai, F., Gandolfi, D., et al. 2018, AJ, 155, 127

Høg, E., Fabricius, C., Makarov, V. V., et al. 2000, A&A, 355, L27

Holman, M. J. & Murray, N. W. 2005, Science, 307, 1288

Hormuth, F., Brandner, W., Hippler, S., & Henning, T. 2008, Journal of Physics Conference Series, 131, 012051

Howell, S. B., Everett, M. E., Sherry, W., Horch, E., & Ciardi, D. R. 2011, AJ, 142, 19

Huang, C. X., Burt, J., Vanderburg, A., et al. 2018, ApJ, 868, L39

Husser, T. O., Wende-von Berg, S., Dreizler, S., et al. 2013, A&A, 553, A6

Irwin, J., Berta, Z. K., Burke, C. J., et al. 2011, ApJ, 727, 56

Jenkins, J. M., Twicken, J. D., McCauliff, S., et al. 2016, in Proc. SPIE, Vol. 9913, Software and Cyberinfrastructure for Astronomy IV, 99133E

Jensen, E. 2013, Tapir: A web interface for transit/eclipse observability, Astrophysics Source Code Library

Jin, S., Mordasini, C., Parmentier, V., et al. 2014, ApJ, 795, 65

Johnson, D. R. H. & Soderblom, D. R. 1987, AJ, 93, 864

Kaminski, A., Trifonov, T., Caballero, J. A., et al. 2018, A&A, 618, A115

Kipping, D. M. 2013, MNRAS, 435, 2152

Kirkpatrick, J. D., Kellogg, K., Schneider, A. C., et al. 2016, ApJS, 224, 36

Kochanek, C. S., Shappee, B. J., Stanek, K. Z., et al. 2017, PASP, 129, 104502

Kreidberg, L. 2015, Publications of the Astronomical Society of the Pacific, 127, 1161

Lafarga, M., Ribas, I., Lovis, C., et al. 2020, arXiv e-prints, arXiv:2003.07471

Lépine, S. & Gaidos, E. 2011, AJ, 142, 138

Lépine, S., Hilton, E. J., Mann, A. W., et al. 2013, AJ, 145, 102

Lépine, S. & Shara, M. M. 2005, AJ, 129, 1483

Lillo-Box, J., Barrado, D., & Bouy, H. 2012, A&A, 546, A10

Lindegren, L., Hernández, J., Bombrun, A., et al. 2018, A&A, 616, A2

Livingston, J. H., Endl, M., Dai, F., et al. 2018, AJ, 156, 78

López, E. D. & Fortney, J. J. 2013, ApJ, 776, 2

Luque, R., Pallé, E., Kossakowski, D., et al. 2019, A&A, 628, A39

López, E. D. & Fortney, J. J. 2014, ApJ, 792, 1

Mann, A. W., Gaidos, E., Vanderburg, A., et al. 2017, AJ, 153, 64

Mathur, S., García, R. A., Régulo, C., et al. 2010, A&A, 511, A46

McCully, C., Volgenau, N. H., Harbeck, D.-R., et al. 2018, in Society of Photo-Optical Instrumentation Engineers (SPIE) Conference Series, Vol. 10707, Proc. SPIE, 107070K

McQuillan, A., Mazeh, T., & Aigrain, S. 2014, ApJS, 211, 24

Montes, D., González-Peinado, R., Tabernero, H. M., et al. 2018, MNRAS, 479, 1332

Morbidelli, A. 2018, arXiv e-prints, arXiv:1803.06708

Mortier, A. & Collier Cameron, A. 2017, A&A, 601, A110

Mortier, A., Faria, J. P., Correia, C. M., Santerne, A., & Santos, N. C. 2015, A&A, 573, A101

Mulders, G. D., Pascucci, I., & Apai, D. 2015, ApJ, 798, 112

Nava, C., López-Morales, M., Haywood, R. D., & Giles, H. A. C. 2020, AJ, 159, 23

Nowak, G., Luque, R., Parviainen, H., et al. 2020, arXiv e-prints, arXiv:2003.01140

Oshagh, M., Santos, N. C., Boisse, I., et al. 2013, A&A, 556, A19

Owen, J. E. & Wu, Y. 2013, ApJ, 775, 105

Owen, J. E. & Wu, Y. 2017, ApJ, 847, 29

Passegger, V. M., Reiners, A., Jeffers, S. V., et al. 2018, A&A, 615, A6

Perger, M., Scandariato, G., Ribas, I., et al. 2019, A&A, 624, A123

Pojmański, G. 1997, Acta Astron., 47, 467

Pollacco, D. L., Skillen, I., Collier Cameron, A., et al. 2006, PASP, 118, 1407

Quirrenbach, A., Amado, P. J., Caballero, J. A., et al. 2014, in Proc. SPIE, Vol. 9147, Ground-based and Airborne Instrumentation for Astronomy V, 91471F

Quirrenbach, A., Amado, P. J., Ribas, I., et al. 2018, in Society of Photo-Optical Instrumentation Engineers (SPIE) Conference Series, Vol. 10702, Ground-based and Airborne Instrumentation for Astronomy VII, 107020W

Reiners, A., Zechmeister, M., Caballero, J. A., et al. 2018, A&A, 612, A49

Ricker, G. R., Winn, J. N., Vanderspek, R., et al. 2015, Journal of Astronomical Telescopes, Instruments, and Systems, 1, 014003

Santos, A. R. G., García, R. A., Mathur, S., et al. 2019, ApJS, 244, 21

Schöfer, P., Jeffers, S. V., Reiners, A., et al. 2019, A&A, 623, A44

Schweitzer, A., Passegger, V. M., Cifuentes, C., et al. 2019, A&A, 625, A68

Scott, N. J. & Howell, S. B. 2018, in Society of Photo-Optical Instrumentation Engineers (SPIE) Conference Series, Vol. 10701, Proc. SPIE, 107010G

Scott, N. J., Howell, S. B., Horch, E. P., & Everett, M. E. 2018, PASP, 130, 054502

Shappee, B. J., Prieto, J. L., Grupe, D., et al. 2014, ApJ, 788, 48

Silverstein, M. L., Schlieder, J., Barclay, T., et al. 2020, in American Astronomical Society Meeting Abstracts, American Astronomical Society Meeting Abstracts, 174.25

Skrutskie, M. F., Cutri, R. M., Stiening, R., et al. 2006, AJ, 131, 1163

Smith, J. C., Stumpe, M. C., Van Cleve, J. E., et al. 2012, PASP, 124, 1000

Southworth, J. 2011, MNRAS, 417, 2166

Stassun, K. G., Oelkers, R. J., Pepper, J., et al. 2018, AJ, 156, 102

Strehl, K. 1902, Astronomische Nachrichten, 158, 89

Stumpe, M. C., Smith, J. C., Catanzarite, J. H., et al. 2014, PASP, 126, 100

Stumpe, M. C., Smith, J. C., Van Cleve, J. E., et al. 2012, PASP, 124, 985

Suissa, G., Chen, J., & Kipping, D. 2018, MNRAS, 476, 2613

Tal-Or, L., Trifonov, T., Zucker, S., Mazeh, T., & Zechmeister, M. 2019, MNRAS, 484, L8

Torrence, C. & Compo, G. P. 1998, Bulletin of the American Meteorological Society, 79, 61

Trifonov, T., Kürster, M., Zechmeister, M., et al. 2018, A&A, 609, A117

Van Eylen, V., Agentoft, C., Lundkvist, M. S., et al. 2018, MNRAS, 479, 4786

Wang, S., Jones, M., Shporer, A., et al. 2019, AJ, 157, 51

Winn, J. N., Petigura, E. A., Morton, T. D., et al. 2017, AJ, 154, 270

Winters, J. G., Medina, A. A., Irwin, J. M., et al. 2019, AJ, 158, 152

Woźniak, P. R., Vestrand, W. T., Akerlof, C. W., et al. 2004, AJ, 127, 2436

Wright, J. T., Marcy, G. W., Butler, R. P., & Vogt, S. S. 2004, ApJS, 152, 261

Wu, Y. 2019, ApJ, 874, 91

Zechmeister, M., Anglada-Escudé, G., & Reiners, A. 2014, A&A, 561, A59

Zechmeister, M. & Kürster, M. 2009, A&A, 496, 577

Zechmeister, M., Reiners, A., Amado, P. J., et al. 2018, A&A, 609, A12

Zeng, L., Jacobsen, S. B., & Sasselov, D. D. 2017, Research Notes of the American Astronomical Society, 1, 32

Zeng, L., Jacobsen, S. B., Sasselov, D. D., et al. 2019, Proceedings of the National Academy of Science, 116, 9723

Zeng, L., Sasselov, D. D., & Jacobsen, S. B. 2016, ApJ, 819, 127

---

[1] Landessternwarte, Zentrum für Astronomie der Universität Heidelberg, Königstuhl 12, 69117 Heidelberg, Germany e-mail: `pbluhm@lsw.uni-heidelberg.de`
[2] Instituto de Astrofísica de Canarias, 38205 La Laguna, Tenerife, Spain
[3] Departamento de Astrofísica, Universidad de La Laguna, 38206 La Laguna, Tenerife, Spain
[4] Space Telescope Science Institute, 3700 San Martin Drive, Baltimore, MD 21218, USA
[5] Centro de Astrobiología (CSIC-INTA), ESAC, Camino bajo del castillo s/n, 28692 Villanueva de la Cañada, Madrid, Spain
[6] Instituto de Astrofísica de Andalucía (CSIC), Glorieta de la Astronomía s/n, 18008 Granada, Spain
[7] Institut für Astrophysik, Georg-August-Universität, Friedrich-Hund-Platz 1, 37077 Göttingen, Germany
[8] Department of Astronomy, University of Tokyo, 7-3-1 Hongo, Bunkyo-ky, Tokyo 113-0033, Japan
[9] Mullard Space Science Laboratory, University College London, Holmbury St. Mary, Dorking, Surrey, RH5 6NT, UK
[10] NASA Goddard Space Flight Center, 8800 Greenbelt Road, Greenbelt, MD 20771, USA
[11] Sellers Exoplanet Environments Collaboration, NASA Goddard Space Flight Center, Greenbelt, MD 20771, USA
[12] Deutsches Zentrum für Luft- und Raumfahrt, Institut für Planetenforschung, 12489 Berlin, Rutherfordstrasse 2., Germany
[13] Centro de Astrobiología (CSIC-INTA), Carretera de Ajalvir km 4, 28850 Torrejón de Ardoz, Madrid, Spain
[14] Department of Physics and Astronomy, George Mason University, 4400 University Drive, Fairfax, VA 22030, USA
[15] Thüringer Landessternwarte Tautenburg, Sternwarte 5, 07778 Tautenburg, Germany
[16] Center for Planetary Systems Habitability and McDonald Observatory, The University of Texas at Austin, Austin, TX 78730, USA
[17] Center for Astrophysics | Harvard & Smithsonian, 60 Garden Street, Cambridge, MA 02138, USA
[18] Departamento de Explotación y Prospección de Minas, Escuela de Minas, Energía y Materiales, Universidad de Oviedo, 33003 Oviedo, Spain
[19] Instituto Universitario de Ciencias y Tecnologías del Espacio de Asturias, Independencia 13, 33004 Oviedo, Spain
[20] Campo Catino Astronomical Observatory, Regione Lazio, 03010 Guarcino (FR), Italy
[21] Leiden Observatory, Leiden University, 2333CA Leiden, The Netherlands
[22] Department of Space, Earth and Environment, Chalmers University of Technology, Onsala Space Observatory, 439 92 Onsala, Sweden
[23] Department of Earth Sciences, University of Hawai'i at Māanoa, Honolulu, HI 96822 USA
[24] IRFU, CEA, Université Paris-Saclay, 91191 Gif-sur-Yvette, France
[25] AIM, CEA, CNRS, Université Paris-Saclay, Université Paris Diderot, Sorbonne Paris Cité, 91191 Gif-sur-Yvette, France
[26] Observatori Astronòmic Albanyà, Camí de Bassegoda s/n, 17733 Albanyà, Girona, Spain
[27] Max-Planck-Institut für Astronomie, Königstuhl 17, 69117 Heidelberg, Germany
[28] Institut de Ciències de l'Espai (ICE, CSIC), Campus UAB, Can Magrans s/n, 08193 Bellaterra, Spain
[29] Institut d'Estudis Espacials de Catalunya (IEEC), 08034 Barcelona, Spain
[30] NASA Ames Research Center, Moffett Field, CA 94035, USA
[31] Department of Physics & Astronomy, Swarthmore College, Swarthmore PA 19081, USA
[32] Astronomical Institute, Czech Academy of Sciences, Fričova 298, 25165, Ondřejov, Czech Republic
[33] Rheinisches Institut für Umweltforschung an der Universität zu Köln, Aachener Strasse 209, 50931 Köln, Germany
[34] Departamento de Física de la Tierra y Astrofísica and IPARCOS-UCM (Instituto de Física de Partículas y del Cosmos de la UCM), Facultad de Ciencias Físicas, Universidad Complutense de Madrid, 28040, Madrid, Spain
[35] Komaba Institute for Science, The University of Tokyo, 3-8-1 Komaba, Meguro, Tokyo 153-8902, Japan
[36] JST, PRESTO, 3-8-1 Komaba, Meguro, Tokyo 153-8902, Japan
[37] Astrobiology Center, 2-21-1 Osawa, Mitaka, Tokyo 181-8588, Japan
[38] Hamburger Sternwarte, Universität Hamburg, Gojenbergsweg 112, 21029 Hamburg, Germany
[39] Homer L. Dodge Department of Physics and Astronomy, University of Oklahoma, 440 West Brooks Street, Norman, OK 73019, USA
[40] Centro Astronómico Hispano-Alemán, Observatorio de Calar Alto, Sierra de los Filabres, 04550 Gérgal, Spain
[41] Zentrum für Astronomie und Astrophysik, Technische Universität Berlin, Hardenbergstr. 36, 10623 Berlin, Germany
[42] Institut für Geologische Wissenschaften, Freie Universität Berlin, Malteserstr. 74–100, 12249 Berlin, Germany
[43] Astronomy Department and Van Vleck Observatory, Wesleyan University, Middletown, CT 06459, USA
[44] Kavli Institute for Astrophysics and Space Research, Massachusetts Institute of Technology, Cambridge, MA 02139, USA
[45] Space Science Institute, 4765 Walnut St., Suite B, Boulder, CO 80301, USA
[46] Department of Earth, Atmospheric and Planetary Sciences, Massachusetts Institute of Technology, Cambridge, MA 02139, USA
[47] Department of Aeronautics and Astronautics, Massachusetts Institute of Technology, 77 Massachusetts Avenue, Cambridge, MA 02139, USA
[48] School of Physics and Astronomy, Queen Mary University London, 327 Mile End Road, London E1 4NS, UK
[49] Department of Physics, Ariel University, Ariel 40700, Israel
[50] Vereniging Voor Sterrenkunde, Brugge, Belgium & Centre for mathematical Plasma-Astrophysics, Department of Mathematics, KU Leuven, Celestijnenlaan 200B, 3001 Heverlee, Belgium
[51] AstroLAB IRIS, Provinciaal Domein "De Palingbeek", Verbrandemolenstraat 5, 8902 Zillebeke, Ieper, Belgium
[52] Department of Physics and Astronomy, Mississippi State University, 355 Lee Boulevard, Mississippi State, MS 39762, USA

Appendix A: Long tables

Table A.1. Priors used for TOI-1235 b in the joint fit with `juliet`.

Parameter[a]	Prior	Units	Description
	Stellar parameters		
$\rho_\star$	$\mathcal{N}(3700, 3800)$	$\mathrm{kg\,m^{-3}}$	Stellar density
	Planet parameters		
P_b	$\mathcal{U}(3, 4)$	d	Period of planet b
$t_{0,b}$	$\mathcal{U}(2458683, 2458687)$	d	Time of transit center of planet b
$r_{1,b}$	$\mathcal{U}(0, 1)$	...	Parameterization for p and b
$r_{2,b}$	$\mathcal{U}(0, 1)$	...	Parameterization for p and b
K_b	$\mathcal{N}(0, 100)$	$\mathrm{m\,s^{-1}}$	RV semi-amplitude of planet b
e_b	0.0 (fixed)	...	Orbital eccentricity of planet b
ω_b	90.0 (fixed)	deg	Periastron angle of planet b
	Photometry parameters		
D_TESS	1.0 (fixed)	...	Dilution factor for *TESS* Sectors 14, 20, 21
$M_\mathrm{TESS,S14}$	$\mathcal{N}(0, 0.1)$	...	Relative flux offset for *TESS* Sector 14
$M_\mathrm{TESS,S20}$	$\mathcal{N}(0, 0.1)$	...	Relative flux offset for *TESS* Sector 20
$M_\mathrm{TESS,S21}$	$\mathcal{N}(0, 0.1)$	...	Relative flux offset for *TESS* Sector 21
$\sigma_\mathrm{TESS,S14}$	$\mathcal{LU}(1, 10^4)$	ppm	Extra jitter term for *TESS* Sector 14
$\sigma_\mathrm{TESS,S20}$	$\mathcal{LU}(1, 10^4)$	ppm	Extra jitter term for *TESS* Sector 20
$\sigma_\mathrm{TESS,S21}$	$\mathcal{LU}(1, 10^4)$	ppm	Extra jitter term *TESS* Sector 21
$q_{1,\mathrm{TESS}}$	$\mathcal{U}(0, 1)$	...	Limb-darkening parameterization for *TESS* Sectors 14, 20, 21
$q_{2,\mathrm{TESS}}$	$\mathcal{U}(0, 1)$	...	Limb-darkening parameterization for *TESS* Sectors 14, 20, 21
D_LCO	1.0 (fixed)	...	Dilution factor for LCOGT
$q_{1,\mathrm{LCO}}$	$\mathcal{U}(0, 1)$	...	Limb-darkening parameterization for LCOGT
M_LCO	$\mathcal{N}(0, 0.1)$	...	Relative flux offset for LCOGT
σ_LCO	$\mathcal{LU}(1, 10000)$	ppm	Extra jitter term for LCOGT
$\theta_{0,\mathrm{LCO}}$	$\mathcal{U}(-100, 100)$	...	Extra jitter term for LCOGT
$\theta_{1,\mathrm{LCO}}$	$\mathcal{U}(-100, 100)$	...	Extra jitter term for LCOGT
	RV parameters		
$\gamma_\mathrm{HARPS-N}$	$\mathcal{N}(0, 10)$	$\mathrm{m\,s^{-1}}$	RV zero point for HARPS-N
$\sigma_\mathrm{HARPS-N}$	$\mathcal{LU}(0.01, 10)$	$\mathrm{m\,s^{-1}}$	Extra jitter term for HARPS-N
γ_CARMENES	$\mathcal{N}(0, 10)$	$\mathrm{m\,s^{-1}}$	RV zero point for CARMENES
σ_CARMENES	$\mathcal{LU}(0.01, 10)$	$\mathrm{m\,s^{-1}}$	Extra jitter term for CARMENES
	GP hyperparameters		
$\sigma_\mathrm{GP,RV}$	$\mathcal{LU}(10^{-10}, 100)$	$\mathrm{m\,s^{-1}}$	Amplitude of GP component for the RVs
$\alpha_\mathrm{GP,RV}$	$\mathcal{LU}(10^{-10}, 100)$	$\mathrm{d^{-2}}$	Inverse length-scale of GP exponential component for the RVs
$\Gamma_\mathrm{GP,RV}$	$\mathcal{LU}(10^{-10}, 100)$	$\mathrm{d^{-2}}$	Amplitude of GP sine-squared component for the RVs
$P_\mathrm{rot;GP,RV}$	$\mathcal{U}(1, 100)$	d	Period of the GP quasi-periodic component for the RVs

Notes. (a) The parameterization for (p, b) was made with (r_1, r_2) as in Espinoza (2018). The prior labels of $\mathcal{N}$, $\mathcal{U}$, and $\mathcal{LU}$ represent normal, uniform, and log-uniform distributions, respectively.

Table A.2. Radial velocity measurements and spectroscopic activity indicators for TOI-1235.

				CARMENES				
BJD (–2450000)	RV ($\mathrm{m\,s^{-1}}$)	CRX ($\mathrm{m\,s^{-1}\,Np^{-1}}$)	dLW ($\mathrm{m^2\,s^{-2}}$)	Hα	Ca IRTa	TiO7050	TiO8430	TiO8860
8796.6533	–1.2±2.2	9±19	–30.4±3.8	0.6954±0.0021	0.5204±0.0022	0.8474±0.0015	0.8656±0.0027	0.9722±0.0028
8807.7240	0.4±2.4	–24±20	–3.2±2.8	0.7004±0.0017	0.5221±0.0018	0.8487±0.0012	0.8694±0.0022	0.9684±0.0023
8811.6588	6.3±2.8	37±25	–22.0±4.1	0.6859±0.0027	0.5194±0.0029	0.8515±0.0020	0.8640±0.0036	0.9746±0.0035
8815.7134	–2.7±1.8	8±15	–0.8±2.0	0.6907±0.0014	0.5294±0.0016	0.8494±0.0011	0.8665±0.0019	0.9742±0.0020
8816.6576	3.0±1.6	–14±13	5.5±2.0	0.6916±0.0013	0.5299±0.0015	0.8859±0.0010	0.8650±0.0018	0.9768±0.0018
8817.7185	0.4±3.2	64±29	–19.3±3.4	0.6973±0.0030	0.5223±0.0035	0.8379±0.0022	0.8542±0.0042	0.9759±0.0042
8831.5414	5.4±2.8	0±23	–4.6±3.3	0.6884±0.0020	0.5199±0.0022	0.8460±0.0015	0.8667±0.0027	0.9770±0.0027
8832.6949	2.5±2.2	–7±19	11.4±3.3	0.6893±0.0018	0.5223±0.0020	0.8486±0.0014	0.8629±0.0025	0.9782±0.0025
8846.6694	–4.2±1.6	16±14	6.3±1.6	0.6894±0.0011	0.5267±0.0013	0.8514±0.0009	0.8666±0.0016	0.9769±0.0017
8848.7121	5.8±1.6	27±13	10.1±1.6	0.6963±0.0011	0.5200±0.0013	0.8489±0.0008	0.8640±0.0015	0.9765±0.0016
8850.6431	2.8±1.4	12±13	1.5±1.9	0.6905±0.0012	0.5256±0.0014	0.8518±0.0009	0.8709±0.0017	0.9761±0.0017
8852.6259	4.5±1.4	9±12	8.0±1.3	0.6989±0.0012	0.5191±0.0014	0.8502±0.0009	0.8687±0.0017	0.9812±0.0017
8854.6620	6.0±2.1	27±14	5.5±1.8	0.6950±0.0011	0.5268±0.0013	0.8488±0.0009	0.8647±0.0016	0.9798±0.0016
8855.6361	4.7±2.0	–3±14	2.5±1.6	0.6864±0.0012	0.5254±0.0013	0.8499±0.0009	0.8678±0.0016	0.9754±0.0016
8856.6278	0.0±1.5	13±11	6.6±1.7	0.6868±0.0011	0.5187±0.0013	0.8523±0.0009	0.8650±0.0015	0.9756±0.0016
8857.6312	–1.5±1.9	6±13	6.1±2.1	0.6952±0.0011	0.5283±0.0013	0.8491±0.0009	0.8666±0.0016	0.9832±0.0016
8858.6017	6.7±2.0	15±16	–2.3±2.5	0.6934±0.0017	0.5265±0.0018	0.8514±0.0013	0.8659±0.0022	0.9826±0.0023
8860.6327	–3.8±1.8	–3±16	2.8±2.3	0.6859±0.0015	0.5227±0.0017	0.8538±0.0012	0.8665±0.0020	0.9769±0.0021
8861.6279	–3.8±1.9	26±15	3.2±2.3	0.6944±0.0014	0.5262±0.0015	0.8506±0.0010	0.8665±0.0019	0.9794±0.0019
8862.6304	–0.2±1.8	27±14	–0.7±1.9	0.6947±0.0014	0.5285±0.0016	0.8509±0.0011	0.8693±0.0019	0.9768±0.0020
8863.6852	–1.4±3.0	–48±27	2.7±3.5	0.6932±0.0021	0.5312±0.0023	0.8470±0.0016	0.8613±0.0028	0.9778±0.0029
8864.6148	–3.8±2.1	–11±16	–6.6±2.4	0.6862±0.0016	0.5217±0.0018	0.8507±0.0012	0.8662±0.0021	0.9758±0.0021
8865.6228	0.6±2.5	–33±23	–5.5±2.6	0.6967±0.0019	0.5277±0.0021	0.8477±0.0014	0.8648±0.0025	0.9864±0.0026
8866.6362	2.0±3.4	–23±28	–4.4±3.5	0.6948±0.0028	0.5287±0.0030	0.8479±0.0020	0.8626±0.0036	0.9867±0.0036
8877.5779	–2.4 ±2.0	–10±13	–4.4±2.2	0.6927±0.0011	0.5219±0.0012	0.8467±0.0008	0.8682±0.0015	0.9839±0.0015
8881.5843	–0.6±1.6	13±15	–8.0±1.9	0.6875±0.0012	0.5185±0.0013	0.8471±0.0009	0.8670±0.0016	0.9821±0.0017
8882.5742	0.3±1.6	2±14	–19.2±2.2	0.6948±0.0014	0.5208±0.0015	0.8493±0.0010	0.8687±0.0018	0.9793±0.0019
8883.5713	–5.9±1.6	1±13	–9.5±1.7	0.6954±0.0012	0.5210±0.0014	0.8485±0.0009	0.8679±0.0017	0.9821±0.0017
8884.5713	–5.5±1.2	2.0±8.8	–4.9±1.6	0.6912±0.0011	0.5151±0.0012	0.8473±0.0008	0.8675±0.0014	0.9756±0.0015
8885.5794	1.2±1.7	–8±13	–5.9±1.8	0.6859±0.0013	0.5209±0.0014	0.8468±0.0010	0.8701±0.0017	0.9804±0.0018
8887.5650	–9.7±3.2	17±27	–9.4±3.7	0.6919±0.0027	0.5260±0.0028	0.8484±0.0020	0.8684±0.0035	0.9772±0.0035
8888.7326	2.2±3.7	12±34	11.0±4.6	0.6912±0.0032	0.5210±0.0034	0.8472±0.0024	0.8611±0.0043	0.9758±0.0041
8890.5100	–0.1±2.8	–37±24	2.3±2.0	0.6939±0.0016	0.5295±0.0018	0.8487±0.0012	0.8651±0.0022	0.9798±0.0022
8890.5332	–1.5±1.8	–19±13	2.2±1.8	0.6884±0.0014	0.5268±0.0016	0.8500±0.0011	0.8668±0.0019	0.9816±0.0020
8891.5446	–2.6±1.5	4±12	6.0±2.4	0.7054±0.0012	0.5305±0.0014	0.8525±0.0009	0.8677±0.0016	0.9872±0.0017
8893.5107	4.1±1.6	4±13	7.9±2.2	0.6982±0.0013	0.5270±0.0014	0.8500±0.0010	0.8705±0.0017	0.9800±0.0018
8894.5328	–1.0±1.9	–24±14	8.1±1.4	0.6911±0.0010	0.5297±0.0011	0.8522±0.0008	0.8678±0.0014	0.9802±0.0015
8895.5580	0.6±2.0	–52±14	–4.9±2.2	0.6938±0.0013	0.5265±0.0014	0.8506±0.0010	0.8706±0.0018	0.9865±0.0018
8896.5272	3.0±1.4	–8±12	0.3±1.9	0.6989±0.0011	0.5233±0.0012	0.8510±0.0008	0.8682±0.0015	0.9784±0.0015
8897.5334	–3.0±1.4	–15±11	1.5±1.5	0.6990±0.0012	0.5270±0.0013	0.8489±0.0009	0.8642±0.0016	0.9877±0.0017
				HARPS-N				
BJD (–2450000)	RV ($\mathrm{m\,s^{-1}}$)	CRX ($\mathrm{m\,s^{-1}\,Np^{-1}}$)	dLW ($\mathrm{m^2\,s^{-2}}$)	Hα	S_{MWO}	$\log R'_{\mathrm{HK}}$		
8862.5810	6.6±2.0	11±17	–12.7±3.5	0.7144±0.0026	0.967±0.043	–4.748±0.045		
8862.7100	2.0±1.0	–2.2±7.5	–25.8±2.0	0.7125±0.0013	0.991±0.014	–4.735±0.038		
8863.6284	0.24±0.60	2.1±4.8	–30.4±1.3	0.7154±0.0010	1.015±0.008	–4.722±0.037		
8863.7378	–1.32±0.72	4.7±5.7	–30.4±1.3	0.7147±0.0009	1.005±0.009	–4.727±0.037		
8864.6070	5.2±1.0	19.5±7.6	–28.4±1.7	0.7144±0.0013	1.000±0.012	–4.730±0.038		
8864.7169	5.91±0.99	7.6±7.8	–30.4±1.6	0.7242±0.0013	1.040±0.014	–4.709±0.038		
8865.5889	8.28±0.70	–0.9±5.7	–29.8±1.4	0.7156±0.0012	1.027±0.010	–4.716±0.037		
8865.7198	4.97±0.76	8.8±6.0	–29.0±1.3	0.7134±0.0011	1.009±0.008	–4.725±0.037		
8869.6175	10.75±0.98	4.5±7.8	–25.9±2.2	0.7131±0.0015	0.986±0.021	–4.738±0.039		
8869.7536	10.22±0.89	–4.2±6.9	–26.1±1.5	0.7152±0.0009	1.073±0.011	–4.692±0.037		
8870.6093	6.0±1.6	–22±13	–22.4±2.4	0.7120±0.0018	1.031±0.030	–4.713±0.040		
8870.6978	6.0±1.6	–21±13	–22.4±2.9	0.7087±0.0020	1.017±0.033	–4.721±0.041		
8895.4528	11.9±1.9	7±15	–27.5±2.8	0.7159±0.0024	0.999±0.042	–4.731±0.044		
8896.5214	11.37±0.95	–2.2±7.5	–31.2±1.9	0.7186±0.0013	0.985±0.016	–4.738±0.038		
8896.6331	12.1±1.2	–2.2±9.6	–31.7±1.8	0.7155±0.0012	1.021±0.014	–4.719±0.038		
8897.6418	4.6±1.1	–14.0±8.4	–34.1±1.5	0.7166±0.0012	0.978±0.012	–4.742±0.038		
8898.5249	6.64±0.87	–16.4±6.4	–35.4±1.3	0.7170±0.0010	1.009±0.010	–4.725±0.037		
8898.6937	2.4±1.0	–8.2±8.2	–35.0±1.8	0.7234±0.0015	0.980±0.019	–4.741±0.039		
8905.5116	–0.8±1.4	2±11	–36.8±2.6	0.7242±0.0018	0.989±0.025	–4.736±0.040		
8905.6346	–0.5±1.6	–8±13	–36.3±2.3	0.7185±0.0020	0.942±0.026	–4.763±0.041		
8925.5936	–5.1±1.5	3±12	–27.1±2.3	0.7183±0.0020	1.033±0.031	–4.712±0.040		